Quantitative Shape Measurements of Distal Volcanic Ash

Colleen M. Riley, William I. Rose, and Gregg J.S. Bluth

(Revised Manuscript Submitted April 15, 2003 to Journal of Geophysical Research)

All from: Department of Geological Engineering and Sciences, Michigan Technological University, 1400 Townsend Drive, Houghton, MI 49931; Phone: (906) 487-2531; Fax: (906) 487-3371

Colleen M. Riley Phone: (360) 694-7093; Email: colleenandahi@hotmail.com

Abstract

Large-scale volcanic eruptions produce fine ash (< 200 μm) which has a long atmospheric residence time (1 hour or more) and can be transported great distances from the volcanic source, thus, becoming a hazard to aircraft and public health. Ash particles have irregular shapes, so data on particle shape, size, and terminal velocities are needed to understand how the irregular-shaped particles affect transport processes and radiative transfer measurements. In this study, a methodology was developed to characterize particle shapes, sizes , and terminal velocities for three ash samples of different compositions. The shape and size of 2,500 particles from 1) distal fallout (~100 km) of the October 14, 1974 Fuego eruption (basaltic), 2) the secondary maxima (~250 km) of the August 18, 1992 Spurr eruption (andesitic), and 3) the Miocene Ash Hollow member, Nebraska (rhyolitic) were measured using image analysis techniques. Samples were sorted into 10 to 19 terminal velocity groups (0.6-59.0 cm/s) using an air elutriation device. Grain size distributions for the samples were measured using laser diffraction. Aspect ratio, feret diameter, and perimeter measurements were found to be the most useful descriptors of how particle shape affects terminal velocity. These measurement values show particle shape differs greatly from a sphere (commonly used in models and algorithms). The diameters of ash particles were 10-120% larger than ideal spheres at the same terminal velocity, indicating that irregular particle shape greatly increases drag. Gas-adsorption derived surface areas are 1 to 2 orders of magnitude higher than calculated surface areas based on measured dimensions and simple geometry, indicating that particle shapes are highly irregular. Correction factors for surface area were derived from the ash sample measurements so that surface areas calculated by assuming spherical particle shapes can be corrected to reflect more realistic values.

Introduction

Large-scale volcanic eruptions that inject ash particles into the stratosphere are a significant hazard to populations both near and far from the volcano as well as aircraft flying through the eruption cloud (Casadevall, 1995; Sparks et al., 1997). The coarser (> 1 mm in diameter) pyroclastic material that is injected into the atmosphere by such an eruption falls out within an hour but remaining finer particles (< 10 μm) can stay suspended for days to months (Rose et al., 2001). These finer particles can be transported great distances and deposit irregularly and in unusually thick amounts far from the volcanic source (Sarna-Wojcicki et al., 1981; Swinehart et al., 1985; Glaze and Self, 1991; Hildreth and Drake, 1992, Ernst et al., 1996). The distance travelled by ash particles is dependent on several factors including particle shape which affects the aerodynamic properties responsible for particle separation and fallout (e.g. Bursik, 1998 for a brief review). Aggregation of particles is also affected because particle surface area, electrostatic charge, and the possibility of mechanical interlocking are related to shape (Gilbert and Lane, 1994). The ability of satellite sensors to accurately quantify ash particle concentrations and effective radius relies on accurate shape characteristics because particle shape may strongly influence electromagnetic scattering (Wen and Rose, 1994; Krotkov et al., 1999b).

Despite their irregular shape, ash particles are most commonly modeled as spheres in both transport modeling experiments (Brazier et al., 1982; Carey and Sigurdsson, 1982; Suzuki, 1983; Armienti et al., 1988; Glaze and Self, 1991; Sparks et al., 1992; Jarzemba et al., 1997) and remote sensing algorithms (Wen and Rose, 1994; Krotkov et al., 1997) primarily because no quantitative description of particle shape has been made. Numerous qualitative SEM studies (summarized in Heiken and Wohletz, 1987) have shown that volcanic particles are generally quite angular and/or irregular and include parachute-shaped bubble-wall shards, equant mineral grains, and subrounded vesicular pumice clasts (Figure 1).

Particle shape assumptions in remote sensing retrieval algorithms influence estimates of particle sizes and ash mass concentrations within an eruption cloud (Mishchenko, 1993; Krotkov et al., 1997; Krotkov et al., 1999b). Both the Total Ozone Mapping Spectrometer (TOMS) and the Advanced Very High Resolution Radiometer (AVHRR), the two most common satellite sensors used to monitor ash clouds, rely on retrieval algorithms for particle size, optical depth, and particle mass concentration. Wen and Rose (1994) state that spherical particle shape assumptions in their algorithm result in overestimation of ash mass concentrations in the volcanic cloud. Krotkov et al. (1999a) used preliminary andesitic ash results from this study to show that spherical particle shape assumptions in radiative transfer algorithms used to interpret TOMS data underestimate the effective particle radius by as much as 30% and overestimate ash cloud optical depth by as much as 25%. Numerical experiments investigating particles as oblate and prolate spheroids show scattering by nonspherical particles differs greatly with scan angle, producing both underestimates and overestimates of ash cloud optical depth (Mishchenko, 1993; Krotkov et al., 1997).

Ashfall particle shape is used to determine terminal velocity rates and ashfall distribution for transport modeling. Particle shape affects the velocity with which a particle will fall from the atmosphere (Stringham et al., 1969; Allen, 1984) and therefore affects how far a particle will be transported by wind. Wilson and Huang (1979) show that the terminal velocities of particles (20-500 μm diameter) can be slowed by orders of magnitude due to particle shape. It is also anticipated that because particle shape affects settling velocities, it should also be accounted for in models of particle reentrainment in eruption columns (Ernst et al., 1996) and in quantitatively assessing the development of settling-driven instabilities in ash clouds (Holasek et al., 1996).

In this study, we characterize the shape and size and determine the terminal velocity of volcanic ash particles for a range of ash compositions. To characterize ash particle shape and size, a methodology which uses air elutriation and image analysis techniques is developed. The data are used to determine which shape, size and compositional factors are the most valuable descriptors of volcanic ash. Eruption information and sample data for these ashes combined with the particle shape, size, and terminal velocity data from this study provide a basis for future studies that will explore the effects of particle shape using transport models and remote sensing measurements.

Eruptions and Ash Samples

Volcan Fuego, Guatemala. The basaltic October 14, 1974 Fuego ash was produced by a sulfur- rich subplinian eruption that reached a height of 18 km above sea level. The eruption injected 0.03 km^3 dense rock equivalent (DRE) of ash into the atmosphere over a period of 5 hours (W.I. Rose, unpublished data). The deposit was well sampled with 51 samples collected between 10-150 km from the volcano, and has been the focus of many studies. Samples were chemically analyzed (Rose, 1977; Rose et al., 1978) and grain size distributions determined (Murrow et al., 1980). The sample chosen for this study was collected within 48 hours of the eruption (S.B. Bonis, Instituto Geográfico Nacional, Guatemala City) at a distal location near the edge of the deposit 150 km from the volcano (Figure 2a).

Mount Spurr, Alaska. The August 18, 1992 Spurr eruption has the most robust data set of the three eruptions in this study (Rose et al., 2001). The volcanic ash and gas clouds from this eruption were tracked and measured by satellites (Wen and Rose, 1994; Bluth et al., 1995; Schneider et al., 1995), and monitored from the ground by radar (Rose et al., 1995) and geophysical observations (Eichelberger et al., 1995). In addition, over 50 fallout samples were collected within 48 hours following the eruption from 2-300 km from the volcano (Neal et al., 1995; Gardner et al., 1998; McGimsey et al., 2001).

The subplinian eruption from the Crater Peak vent at Mount Spurr erupted 14 X 10^6 m^3 dense rock equivalent (DRE) of pyroclastic material (Neal et al., 1995; Gardner et al., 1998). The plume reached the stratosphere at a peak altitude of at least 13.7 km above sea level, as detected by radar (Rose et al., 1995), and traveled eastward in the prevailing wind direction (Schneider et al., 1995; Rose et al., 2001). A bulk deposit isomass map (Figure 2b) for this eruption shows that the tephra deposit contains an area of secondary thickening ~ 200 km away from the volcanic source (McGimsey et al., 2001).

The sample used in this study was collected approximately 225 km ESE of Spurr near Wells Bay (McGimsey et al., 2001). The ash was deposited in this area 7-8 hours after the start of the eruption based on reports and observations of ash falling in nearby areas (Eichelberger et al., 1995).

Ash Hollow Member, Nebraska. The late Miocene (9-11 Ma) Ogallala Formation contains at least ten ash members which extend from Nebraska to Texas, covering 1000s of square kilometers (Frye et al., 1956). The Ash Hollow Member is the topmost ash unit of the Ogallala Formation and is of rhyolitic composition (Swinehart et al., 1985). The source of this ash is unknown (Figure 2c), but the formation age corresponds to the time of activity of the Bruneau-Jarbridge center of the Snake River Plain (Perkins et al., 1995; Perkins, 2001, personal communication). The distribution of this ash deposit (Figure 2c) is difficult to map since the ash was partially redistributed by wind and water into deposit thicknesses of up to 22 m (Swinehart et al., 1985), and the multiple ash layers deposited in this area require chemical analyses in order to trace separate ash layers (Perkins, 2001, personal communication). The ash extent shown in Figure 2c is only an estimate of where ash may have been deposited if erupted from the Bruneau-Jarbridge center.

The ash sample used in this study was collected from the Ash Hollow member in southwestern Nebraska near Broadwater where it is ~1m thick and overlies a 2.5-3 m thick conglomerate. The sample was collected 40-70 cm from the top of the deposit where the ash is laminated (1-2 cm thick layers) and where there was a layer of accretionary lapilli that individually measured 5-7 mm in diameter. The sampled outcrop showed the least fluvial influence of all the outcrops sampled, and the ash particles showed few effects from weathering.

Methods

Grain size distributions for the bulk samples of all three ashes were measured by Malvern Instruments Ltd. using the Malvern Mastersizer 2000 laser diffraction instrument (Appendix A[1]; Malvern Instruments Ltd., 2000; Rawle, 2000a and 2000b). An air elutriation device called the Roller particle size analyzer (Appendix B[1]; Roller 1931a and 1931b) was used to sort the ash samples into terminal velocity groups. The air flow rates used to sort the samples were incorporated into the Stoke's law equation (since airflow through the Roller analyzer is laminar) and terminal velocities were determined for the sorted groups (Appendix C[1]). While sorting the sample some of the particles in the lowest three terminal velocity groups (0.6-3.7 cm/s) clumped together to form aggregates (Appendix D[1]), which may introduce some error in the shape measurements. The ash particles in each terminal velocity group were applied to aluminum stubs for use with the scanning electron microscope (Appendix E[1]). Two to seven backscattered images containing totals of 27 to 145 individual particles were collected for each terminal velocity group using a Jeol JXA-8600 electron microprobe analyzer (Appendix F[1]). Bit maps were made of the

1. Supporting material is available via Web browser or via Anonymous FTP from ftp://ftp.agu.org, directory "apend" (Username = "anonymous", Password = "guest"); subdirectories in the ftp site are arranged by paper number. Information on searching and submitting electronic supplements is found at http:// www.agu.org/ pubs/esupp_about.html.

particles in each image and shape and size measurements (Table 1) were made by an automated image analysis program called Clemex Vision ™ (Appendix F[1]). Surface areas for bulk samples of the three ashes were also made using the BET (Brunauer, Emmett, and Teller) method (Appendix G[1]; Brunauer, 1945).

Results

Physical Description of Particles

Fuego. A total of 1,300 particles were measured by SEM imagery in the various Roller splits for the Fuego sample (Figure 3a) and categorized as 1) vesicular, 2) non-vesicular, and 3) miscellaneous particles (Appendix H[1]). The bulk of the Fuego sample is composed of non-vesicular glass (75%), perhaps containing microphenocrysts. The rest of the sample is composed of basaltic pumice clasts (25%) having 38% vesicles, and trace amounts of other particles that could not be identified (Appendix H[1]). Previous studies (Rose et al., 1978) have shown that coarser juvenile particles (> 200 μm) in the Fuego fall deposits contain 38% phenocrysts, including olivine, magnetite, augite, and amphibole. These phenocrysts are typically far larger than 200 μm in diameter and are rare or absent in the fine-grained fall sample studied here. Both vesicular and non-vesicular particles have a high electron beam reflectance in backscatter images and so appear bright in the images (Figure 3a).

Mount Spurr. Approximately 1,300 particles were measured for the August 18, 1992 Spurr fallout sample (Figure 3b). The majority of the vesicular particles are andesitic pumice clasts that have 20-40% vesicles. These vesicular clasts are generally larger than the non-vesicular particles (perhaps because the non-vesicular particles are fragments of the larger vesicular clasts) and gray or tan in color. Images of the vesicular particles show that they contain small crystals, called microlites, of plagioclase and pyroxene (Gardner et al., 1998). The majority of non-vesicular particles are glass bubble-wall shards with microlites, and make up 44% of all the measured particles. Trace amounts of "other" particles, probably mineral ("dust") grains, were measured, but due to the rarity of these particles are considered environmental contaminants (Appendix H[1]) and ignored in this study.

Ash Hollow. Over 850 particles were measured for the Ash Hollow sample (Figure 3c). The sample is composed almost totally of bubble-wall shards (> 99%) and has no pumice clasts (Appendix H[1]). The glass shards are platy and have small thicknesses (~20 μm) compared to their widths (~110-140 μm) and often show distinct bubble junctions and bubble-wall curvatures. No phenocrysts were observed within the glass or as individual particles.

Chemical Composition of Particles

Appendix I[1] shows compositional data and references which give detailed information on the three ashes studied. The 1974 Fuego magma is a high-aluminum basalt with substantial phenocryst content (W.I. Rose, unpublished data). The sample studied is distal (~150 km from the volcano) and reflects preferential fallout of large phenocrysts. The Spurr magma is calcalkalic andesite with a slightly lower crystal content than Fuego (Gardner et al., 1998). The sample studied is distal (~250 km from the volcano) and has probably also lost most or all of its phenocrysts in near-source fallout. Both Fuego and Spurr have hypocrystalline to hyalocrystalline groundmass components (W.I. Rose, unpublished data; Gardner et al., 1998), which are the dominant components of the ashes studied. The Ash Hollow sample is composed completely of homogenous hydrated rhyolitic glass.

Grain Size Distribution Results

Grain size distribution results for the Fuego sample (Figure 4a) show the sample is unimodal, poorly-sorted according to sedimentological standards (though is well-sorted as compared to most volcanic ash samples), and has a high skewness, indicating that a high proportion of the sample is within the fine-grained tail (Table 2). This is contrary to a previous study which obtained less detailed grain size data on the same ash sample using Coulter-counter and sieves (Murrow et al., 1980) and showed a weakly bimodal distribution. The change in measurement devices for coarse and fine particles in that study probably introduced some error which made the sample look bimodal. The precise measurements and range of sizes that laser diffraction devices can measure (0-2000 μm), make their data superior to the older sieve and Coulter-counter methods.

The grain size distribution of the Spurr sample, as indicated by laser diffraction methods, is bimodal (Figure 4b) with peaks at 3.5 and 5.5 ϕ (88 and 22 μm). The sample is sedimentologically poorly-sorted and has a prominent fine tail (Table 2). Grain size distribution results for the Ash Hollow sample (Figure 4c) show that the sample is unimodal, sedimentologically poorly-sorted, and rich in fine particles < 100 μm in diameter (Table 2).

Quantitative Shape Measurements

All the particle shape and size results are listed in Appendices J-L[1] and summarized in Table 3. The various parameters measured for each particle are tabulated in measurement categories of shape and size. Data for individual particles were separated into non-vesicular and vesicular particle groups for the Fuego and Spurr samples. By separating the particles into groups, we aim to provide greater detail on how particle shape and size affect terminal velocity versus using group means. Three types of means were calculated for each parameter in each terminal velocity group: 1) a combined mean which uses measurement data from both non-vesicular and vesicular particle types, 2) a vesicular mean, and 3) a non-vesicular mean. Combined, vesicular, and non-vesicular means for shape and size parameter measurements are given in Appendix J[1] for Fuego and Appendix K[1] for Spurr. The Ash Hollow, NE sample only contained non-vesicular particles (Appendix L[1]).

Image Processing Measurements

The pattern observed for the shape parameter feret average (the average of 64 diameter measurements for a single particle; Table 1) is similar to patterns observed for perimeter, length, and area, and shows that measurements increase in parabolic fashion with increasing terminal velocity in all ash samples (Figure 5a). For all these parameters, Ash Hollow measurements plot above Spurr and Fuego, reflecting their more complex shape. The pattern observed in aspect ratio data is (Figure 5b) flat for Spurr and Fuego, but varies for Ash Hollow. Ash Hollow values are usually higher than Spurr and Fuego values. Results for sphericity and roughness do not have clear patterns with increasing terminal velocity, though values are constrained between 0.6-0.8 for sphericity and 0.9-1.0 for roughness in all ash samples.

Figure 6 compares measured terminal velocities of some of the size parameters to calculated terminal velocities assuming a spherical shape. Generally, the curves are steeper for smaller particles and flatten as the size of particles increase. Measured diameters at specific terminal velocities for Ash Hollow are larger than those for Spurr and Fuego.

Non-vesicular and Vesicular Mean Results

Non-vesicular and vesicular means were compared for Fuego (Figure 7) and Spurr (Figure 8) samples. The Ash Hollow sample contained only non-vesicular particles. Patterns for feret average (Figure 7 and 8a) are similar to those for area, perimeter, and length and show that vesicular particles generally have higher mean values than non-vesicular particles except for the lower terminal velocity groups of Fuego (TV < 18 cm/s). The Fuego curves do not show as much variability between non-vesicular and vesicular particles within individual TV groups as Spurr. The differences between vesicular and non-vesicular values in all curves for both Fuego and Spurr samples become greater as terminal velocity increases.

Non-vesicular fractions of both ash samples generally show higher values of aspect ratio (Figures 7 and 8b), compactness, sphericity, and roughness than vesicular fractions. For aspect ratio, both the Spurr and Fuego samples have more variability in their highest velocity groups.

BET Surface Area Results

BET surface area results are (Table 3) up to 100 times greater than those calculated for surface areas of various geometrical shapes (Figure 9) using our measurements for feret average, length, and width. Even the more reasonable surface area calculations (using cylinders for Fuego and Spurr and a disk for Ash Hollow) which lie closest to the BET values only account for 30 to 50% of the surface area of the ash.

Discussion

We have described shape and size measurements from Spurr, Fuego, and Ash Hollow samples with the goal of explaining how ash particle shape influences terminal velocity and remote sensing radiance measurements. We have generated numerical results and will now investigate how we can use them.

The basic data we have generated, without any further calculations or manipulations, are profound in their statements about particle shape in volcanic fallout. 1.) The ash sample that travelled the greatest distance, Ash Hollow, contains the coarsest particles (Table 2). Although it is clear from the huge inferred extent of the Ash Hollow airfall that it corresponds to an eruption of much higher intensity (and column height) than either the Fuego or Spurr cases, it is still surprising that the Ash Hollow deposit is so coarse at ~1200 km from the source. This highlights that particle size (with wind speed and column height accounted for) is inadequate to characterize ash dispersal and model it. Particle shape can play as important a role as these other factors and should be carefully considered in future studies. 2.) At identical terminal velocities the three ash samples studied vary markedly in density, area, perimeter, length, width, feret average, aspect ratio, and compactness. This shows that we can measure highly variable shape aspects. 3.) The extreme difference between measured and calculated surface areas combined with SEM observations of the ash samples indicate that there is a significant surface area contribution from fine scale roughness, porosity, and the irregular shapes of volcanic ash which is likely to significantly affect chemical processes, electrostatic aggregation, and scattering phenomena in the volcanic cloud.

Which image processing measurements are most useful for predicting terminal velocity?

The relationship between particle shape and drag is not well understood, despite many experimental and theoretical studies. Most studies have focused on coarse particles with simple geometrical shapes (spheres, disks, cubes, prolate spheroids, oblate spheroids, etc.) [e.g. Schmiedel, 1928; Pettyjohn and Christiansen, 1948; McNown and Maliaika, 1950; Jayaweera and Mason, 1965; Stringham et al., 1969; Allen, 1984]. A few experiments measured the actual settling rates of irregular-shaped volcanic and sedimentary particles (Fisher, 1964; Walker et al., 1971; Komar and Reimers, 1978; Wilson and Huang, 1979). Walker et al. (1971) measured terminal velocities of various pyroclasts and showed that their fallout rates were similar to theoretically determined terminal velocities for cylinders. Wilson and Huang (1979) measured the terminal velocity of glass, pumice, and feldspar particles (30-500 μm) from ashfall materials.

They also measured each particle's diameter along three axes and found differences of orders of magnitude in terminal velocity related to particle shape and atmospheric drag.

In this study, particles are characterized by a wide range of shape and size parameters and their terminal velocities are directly measured. The most useful measured parameters found by this study for predicting terminal velocity are believed to be the feret average, aspect ratio, sphericity, and roughness (see Table 1 and 3).

Which shape parameters are the best shape descriptors?

The difference between the three ashes studied is shown clearly by the aspect ratio and feret average (Figure 5). The Spurr and Fuego samples show similar size and shape trends overall which matches their visual similarity (Figure 3a and b), but the Ash Hollow sample is dramatically different (Figure 3c), having a much steeper increase in measured values with increasing terminal velocity and higher values than the other two ashes.

For remote sensing applications, we have been able to use the aspect ratio data to improve calculations for effective radius and volcanic cloud mass concentrations (see Krotkov et al., 1999b). The aspect ratio tells us about the shape and surface area of a particle. The wide variability in aspect ratios measured for non-vesicular particles of the Ash Hollow sample, and low terminal velocity particles in the Spurr and Fuego samples, suggest that these particles have shapes whose form is greatly influenced by relict bubble-walls (fragmentation by expanding gases in the magma would cause breakage along irregularly distributed vesicles and concave-shaped bubble-walls).

For the estimation of surface area, the best descriptors may be perimeter and convex perimeter, which are used to determine sphericity, compactness, and roughness (Table 1). The surface area of ash is important in issues of charging and aggregation (Lane and Gilbert, 1992; Gilbert and

Lane, 1994) and also in the kinetics of heterogeneous chemical reactions such as the conversion of SO_2 to sulfate (Schneider et al., 1999). Surface area is also important to particle fallout since more surface area means greater contact with the atmosphere which produces greater drag, resulting in greater transport distance from the source (for a given eruption intensity). Since the perimeter and convex perimeter values are similar, the sphericity and compactness measurements do not differ greatly. If the particles had greater changes in their surface topography (greater roughness), sphericity and compactness values would be more distinct. These measurements show the Ash Hollow particles have the greatest surface area.

Figure 10 compares the measured perimeters for all ashes to the calculated equivalent perimeters of spheres at the same terminal velocity. The measured perimeters are 1.5 to 2 times larger than calculated perimeters.

How can image processing measurements be used to predict surface area?

The surface area of a sphere is easily related to the diameter by πd^2, so the feret average can be used as "diameter" to convert to an equivalent spherical surface area, which will always be less than the real surface area (sphere density is assumed to equal the same density as the volcanic ash compositon). Surface areas calculated by this method for the ash samples were shown in Figure 9. The comparison of these calculated surface areas to BET derived surface areas showed the calculated surface areas were substantially lower by a factor of 1 to 2. The "missing" surface area comes from particle porosity, fine roughness, and the irregular shapes of particles which cannot be described completely by simple geometric shapes or two-dimensional image analysis methods. The calculation for surface area of the Ash Hollow sample was greatly improved by using a disk to represent the shapes of the thin glass shards. This also emphasizes the importance of particle shape in surface area calculations.

It would be useful to have a factor which would adjust the calculated surface area values to reflect the true surface areas as determined by BET analysis. Such a correction factor (F) for spheres (the shape most commonly used by modelers) of a specific composition can be determined using the ratio of BET surface area to calculated surface area assuming spherical shape (Table 4).

The correction factors were tested by using the particle radii (r) from laser diffraction grain size distributions and Coulter counter/sieve measurements of the ash samples. Perimeters of spherical particles ($2\pi r$) were calculated and surface areas (2r X Perimeter) determined for each particle. The total calculated surface area was multiplied by the correction factor most appropriate for the ash composition used (Table 4). Surface area results were within a factor of two or better to the values determined using BET analysis. The corrected surface area for Fuego using sieve and Coulter-counter data greatly overestimated surface area, whereas, the Mastersizer results were much closer to the BET value, which emphasizes the importance of obtaining detailed and accurate grain size data.

The surface area ratios are much greater than the perimeter ratios, especially for the Ash Hollow sample (Figure 11). This emphasizes that the irregular shapes of ash particles are not accurately described by 2-D measurements like perimeter. The simple geometric shapes used are poor descriptors of the real particle shapes. The disk used for Ash Hollow was closest to the BET measured values.

Which particle size measurements are the most useful?

Many methods of shape classification have been developed which use particle diameter (Wadell, 1932; Zingg, 1935; Corey, 1949). These methods were considered by Wilson and Huang (1979) who describe particle shape using the shape factor, SF,

$$SF=(b+c)/2a$$

where a, b, and c represent the longest, intermediate, and short particle axes, respectively.

We used the values for feret diameter to determine the Wilson and Huang (1979) shape factor, F, since this factor has been used in several transport models (Suzuki, 1983; Glaze and Self, 1991; CNWRA, 1997). The values used for long, intermediate, and short axes are length, feret average, and width, respectively. Our results show that the shape factor is 0.7-0.8 for Fuego and Spurr and 0.6-0.7 for Ash Hollow (see Appendices J-L[1]). This compares to a shape factor value of 0.5 which was determined by Wilson and Huang (1979) for the volcanic particles they studied (rhyolite ash from the Toba eruption).

In order to determine how particle shape affects fallout, density influences need to be separated from shape influences. The terminal velocities of perfect spheres were compared at various densities with the ash size data (Figure 6, 7a, 8a).

Measurements of Spurr pumice densities were made by Gardner et al. (1998) using the Hoblitt and Harmon (1993) method on ash deposited near the volcanic source (< 15 km). These deposits contain two types of pumice clasts that differ in density, vesicularity, and color but not in chemical composition (Neal et al., 1995). Tan pumice clasts are found at the bottom of the deposit and grade to gray pumice clasts at the top of the deposit (Neal et al., 1995). Gardner et al. (1998) determined that the tan pumice clasts had densities of 1.5-1.7 g/cm^3 and that the gray pumice clasts had densities of 2.1-2.3 g/cm^3. The Spurr ash sample used in this study contained both tan and gray pumice clasts, so we compared the data to density curves based on both of Gardner’s estimates (Figure 6b and 8a).

The bulk density of the Fuego ashfall has been estimated in the field at 1.14 g/cm^3 (W.I. Rose, unpublished data). The density of individual ash particles is much higher than this estimate, however. The sample contains both non-vesicular and vesicular clasts, so we compared the shape measurements to density curves (Figure 6a and 7a) using a density of 2.4-2.6 g/cm^3 for the non-vesicular basalt clasts (Fisher, 1964; Brazier et al., 1982).

Particle density for Ash Hollow particles (Figure 6c) has not been precisely determined, but the particles are non-vesicular and so their density is assumed to approximate rhyolitic glass (2.3 g/cm^3, Williams et al., 1954).

Our measurements (Figure 6, 7a, 8a) show that particles are falling out at slower velocities than predicted by the density curves, indicating that particle shape greatly increases drag. Extrapolation of the appropriate density curves indicates large particles are falling out at terminal velocities that are slower by factors of up to 10 or more. The shape and drag affects all three ash samples, becomes more marked for larger particles, and is greatest for the Ash Hollow sample which is the ash with the most extreme aspect ratio.

Another way to consider shape effects on fall velocity is to calculate the diameter of perfect spherical particles that would fall at the same terminal velocity as the ash particle groups (tabulated in Appendix M[1]). These diameters are plotted in Figure 12 and compared to feret averages for the three ash samples studied. Data show that the feret averages are much greater than ideal spherical particle diameters, indicating that shape causes particles to fall at a considerably slower rate. Feret diameters in the lowest velocity groups are smaller than the spherical particles for Spurr and Fuego. These results are probably due to aggregation in the settling chamber which would cause the small particles (as part of an aggregate) to fall out at higher terminal velocities than they would normally have if they were travelling individually. This hypothesis is supported by the collection of aggregates in the settling chamber at low flow rates.

How are the shapes of Spurr particles affected by vesicles and phenocrysts?

During our analysis of the particle measurements area, perimeter, feret average (Figure 8a), and various other diameters (Figure 6b), we noticed that the combined mean curves for Spurr had unusual peaks at TV =21.5 cm/s and TV =38.1 cm/s. These have equivalent feret averages of ~100 μm and 125 μm. The peak at TV =38.1 cm/s is most likely statistical, reflecting the small number of non-vesicular particles measured in this group (<10%; Appendix H[1]), resulting in large error for the non-vesicular mean. The peak at TV =21.5 cm/s is not statistical, since > 17% of the particles measured were non-vesicular. We ruled out experimental factors for this peak since it does not correlate to any changes in flow rate, chamber diameter, or nozzle size, and the collection procedure was the same as for other settling groups (Appendix B[1]). The peak may reflect fragmentation mechanisms controlled by the size, density and geometry of vesicles and phenocrysts in the magma (Heiken and Wohletz, 1985). To investigate this, we compiled the average size of vesicles and phenocrysts from thin section images of gray and tan pumice clasts for the August 18, 1992 Spurr eruption (Cynthia Gardner, unpublished data). Average vesicle sizes ranged between 13-24 μm. Most vesicles were ~20 μm in diameter but a few were as large as 40-120 μm. Mafic phenocryst sizes had an average length of 86 μm and an average width of 52 μm. Plagioclase phenocryst sizes had an average length of 154 μm and an average width of 75 μm.

Vesicle diameters of about 20 μm explain the abundance of non-vesicular particles in smaller size fractions of the Spurr ashes. Particles larger than the vesicle sizes tend to be in the vesicular class and likely have a lower density. Fragmentation for particles with feret averages of 20-80 μm (TV 3.7-18 cm/s) would be affected by the size of mafic phenocrysts, large vesicles, and small plagioclase phenocrysts, because breakage of these phenocrysts is less likely than simple liberation (breakage along edges). Fragmentation for larger particles >80 μm (TV >18 cm/s) would be primarily influenced by the size of abundant plagioclase phenocrysts. The peak at ~100 μm (TV = 21.5 cm/s) thus reflects the existence of a phenocryst population of approximately that size which tends to be liberated, rather than breaking. So, the peaks in the combined mean curves for Spurr reveal important information regarding fragmentation mechanisms which, in turn, determine the shapes of particles.

Neither the Fuego or Ash Hollow samples had noticeable peaks in their shape and size parameter curves. For Fuego, phenocrysts are much larger (> 200 μm) and are likely to have been subject to rapid turbulent flow fallout which makes them absent from the distal sample studied. In the case of Ash Hollow, there are no obvious phenocrysts and presumably this reflects either an aphyric magma or large phenocrysts lost by fallout, as in the case of Fuego.

Conclusions

To improve our understanding of volcanic ash transport and remote sensing measurements of volcanic clouds, we need quantitative data for fine ash particle shapes (< 200 μm diameter). This study developed an accurate methodology for characterizing the shape and size of individual fine ash particles using image analysis. In addition, the terminal velocities of these particles were measured using an air elutriation device called the Roller analyzer. To demonstrate the method on a variety of ashes, we studied distal fallout particles from basalt (Fuego, 1974), andesite (Spurr, 1992), and rhyolite (Ash Hollow, Miocene) eruptions.

The most distinctive shape parameter measured was aspect ratio, which varied greatly from a sphere (1.0) and was 1.5 for the andesitic and basaltic ashes and 1.5-2.6 for the rhyolitic ash. Roughness and sphericity parameters, which use measurements of perimeter and convex perimeter, also provided important shape information. Particle roughness values were similar for all ashes (0.9-1.0 for Spurr and Fuego, and 1.0 for Ash Hollow) and close to 1.0, but even small changes in surface roughness (<10%) could significantly affect terminal velocity. Sphericities

(0.6-0.9 for Spurr, 0.6-0.8 for Fuego and Ash Hollow) showed particles differed greatly from a sphere (1.0).

The most useful size parameter is feret diameter since it measures the particle in 64 directions to get an average diameter. The feret diameter measurements for the three ash samples were compared with the diameter of spheres which would fall at the same terminal velocity as that measured for the ashes. The ideal spheres were larger than the ash at fine sizes (feret diameter < 25 μm) due to aggregation in the Roller analyzer. Coarser ash was 10-60%, 10-80%, and 40-120% larger (basalt, andesite, and rhyolite, respectively) than ideal spheres.

BET surface areas of fine ashes were as much as one (rarely two) orders of magnitude greater than calculated values for particles using simplified geometric shapes, suggesting that the irregular shapes of ash particles and porosities contribute greatly to surface area. Correction factors (F) for three ash compositions, which relate calculated surface areas to real surface areas, were derived (F=14 for Fuego, F=7 for Spurr, and F=38 for Ash Hollow) and provide a useful way for researchers using similar ash compositions to estimate surface area. Measured perimeters were found to be 1.5 (Spurr and Fuego) to 2 (Ash Hollow) times greater than calculated spherical equivalent perimeters.

One of the ash samples studied (Spurr) showed that phenocrysts and vesicles influenced fragmentation and were important determinants of the resulting shape and size of particles. Thus size distribution data for ashes should be accompanied by information about vesicles, phenocrysts, and microphenocrysts.

Acknowledgements

Funding for this work was provided by the NASA Graduate Student Researchers' Program and Michigan Space Grant Consortium. We would like to thank Game McGimsey and Cynthia

Gardner for providing valuable information, data, and ash samples for Spurr. Bob Diffendal gave us a guided tour of the Ogallala formation deposits and Mike Perkins provided us with ash chemistry data for these deposits. Sam Bonis collected the sample from Fuego and Pat Murrow provided grain size data. Thanks to Nick Krotkov and Arlin Krueger for several discussions regarding remote sensing implications of this work. Owen Mills and Yingxin Gu provided BET measurements for the samples. Special thanks to Owen Mills, Tim Eisele, and Komar Kawatra for their assistance with equipment and data collection. Thanks to Larry Mastin, Grant Heiken, Gerald Ernst, and Francis Albarede whose comments greatly improved the manuscript.

References

Allen, J.R.L., *Sedimentary Structures: Their Character and Physical Basis*, v. 1, Elsevier, 183-188, 1984.

Armienti, P., G. Macedonio, and M.T. Pareschi, A numerical model for simulation of tephra transport and deposition: Applications to May 18, 1980, Mount St. Helens eruption, *J. Geophys. Res.*, 93, 6463-6476, 1988.

Bluth, G.J.S., C.J. Scott, I.E. Sprod, C.C. Schnetzler, A.J. Krueger, and L.S. Walter, Explosive SO2 emissions from the 1992 eruptions of Mount Spurr, Alaska., *USGS Bull.*, 2139, 37-45, 1995.

Bonadonna, C., G.G.J. Ernst, and R.S.J. Sparks, Thickness variations and volume estimates of tephra fall deposits: the importance of particle Reynolds number, *J. Volc. and Geo. Res.*, 81, 173-187, 1998.

Brazier, S., A.N. Davis, H. Sigurdsson, and R.S.J. Sparks, Fallout and deposition of volcanic ash during the 1979 explosive eruption of the Soufriere of St. Vincent, *J. Volc. and Geo. Res.*, 14, 335-359, 1982.

Brunauer, S., Physical adsorption, Princeton University Press, Princeton, N. J., 1945.

Bursik, M.I., in J.S Gilbert and R.S.J. Sparks (eds.), The physics of explosive eruptions, *Geol. Soc. Spec. Publ. 145*, 115-144, 1998.

Carey, S. and H. Sigurdsson, Influence of particle aggregation on deposition of distal tephra from the May 18, 1980, eruption of Mount St. Helens Volcano, *J. Geophys. Res.*, 87, 7061-7072, 1982.

Casadevall, T.J. and M.D. Krohn, Effects of the 1992 Crater Peak eruptions on airports and aviation operations in the United States and Canada, *USGS Bull. 2139*, 205-220, 1995.

Corey, A.T., Influence of shape on the fall velocity of sand grains, *M.S. Thesis*, Colorado A&M College, 1949.

CNWRA (Center for Nuclear Waste Regulatory Analyses), Ashplume version 1.0--A code for contaminated ash dispersal and deposition, 1997.

Eichelberger, J.C., T.E.C. Keith, T.P. Miller, and C.S. Nye, The 1992 eruptions of Crater Peak Vent, Mount Spurr Volcano, Alaska: Chronology and Summary, *USGS Bull.*, 2139, 1-18, 1995.

Ernst, G.G.J., M.I. Bursik, S.N. Carey, and R.R.J. Sparks, Sedimentation from turbulent jets and plumes, *J. Geophys. Res.*, *101*, 5575-5589, 1996.

Fisher, R.V., Settling velocity of glass shards, *Deep-Sea Res.*, 12, 345-353, 1964.

Frye, J.C., A.B. Leonard, and A. Swineford, Stratigraphy of the Ogallala Formation (Neogene) of Northern Kansas, *State Geological Survey of Kansas Bulletin 118*, 90 p., 1995.

Gardner, C.A., K.V. Cashman, and C.A. Neal, Tephra-fall deposits from the 1992 eruption of Crater Peak, Alaska: implications of clast textures for eruptive processes, *Bull. Volcanol.*, 59, 537-555, 1998.

Glaze, L.S. and S. Self, Ashfall dispersal for the 16 September, 1986 eruption of Lascar, Chile, calculated by a turbulent diffusion model, *Geophys. Res. Let.*, *18*, 1237-1240, 1991.

Gilbert, J.S. and S.J. Lane, The origin of accretionary lapilli, *Bull. Volcanol.*, *56*, 398-411, 1994.

Heiken, G. and K. Wohletz, *Volcanic Ash*, University of California Press: Berkeley, 246, 1987.

Hildreth, W. and R.E. Drake, Volcan Quizapu, Chilean Andes, *Bull. Volcanol.*, *54*, 93-125, 1992.

Hoblitt, R.P. and R.S. Harmon, Bimodal density distribution of cryptodome dacite from the 1980 eruption of Mount St. Helens, Washington, *Bull. Volcanol.*, *55*, 421-437, 1993.

Holasek, R.E., A.W. Woods, and S. Self, Experiments on gas-ash separation processes in volcanic umbrella clouds, *J. Volc. and Geo. Res.*, *70*, 169-181, 1996.

Jarzemba, M.S., P.A. LaPlante, and K.J. Poor, *Ashplume version 1.0--A code for contaminated ash dispersal and deposition: Technical description and user's guide*, Center for Nuclear Waste Regulatory Analyses, San Antonio, TX, 1997.

Jayaweera, K.O.L.F. and B.J. Mason, The behaviour of freely falling cylinders and cones in a viscous fluid, *J. Fluid Mech.*, 22, 709-720, 1965.

Komar, P.D. and C.E. Reimers, Grain shape effects on settling rates, *J. Geology*, 86, 193-209, 1978.

Krotkov, N.A., D.E. Flittner, A.J. Krueger, A. Kostinski, C. Riley, W.I. Rose, and O. Torres, Effect of particle non-sphericity on satellite monitoring of drifting volcanic ash clouds, *J. Quant. Spectrosc. Radiat. Transfer, 63, 613-630*, 1999a.

Krotkov, N.A., O. Torres, C. Seftor, A.J. Kruegar, A. Kostinski, W.I. Rose, G.J.S. Bluth, D. Schneider, S.J. Schaefer, Comparison of TOMS and AVHRR volcanic ash retrievals from the August 1992 eruption of Mt. Spurr, *Geophys Res. Let.*, 26, 455-458, 1999b.

Krotkov, N.A., A.J. Krueger, and P.K. Bhartia, Ultraviolet optical model of volcanic clouds for remote sensing of ash and sulfur dioxide, *J. Geophys. Res*., 102, 21,891-21,904, 1997.

Lane, S.J. and J.S. Gilbert, Electric potential gradient changes during explosive activity at Sakurajima volcano, Japan, *Bull. Volcanol., 54,* 590-594, 1992.

Malvern Instruments Ltd, Laser diffraction for particle size analysis-why use Mie theory?, *LabPlus International*, available from the World Wide Web server at http://www.malvern.co.uk, 2000.

McGimsey, R. G., C.A. Neal, and C.M. Riley, Areal distribution, thickness, mass, volume, and grain size of tephra-fall deposits from the 1992 eruptions of Crater Peak vent, Mt. Spurr volcano, Alaska, *USGS Open-File Rep. 01-370*, 2001.

McNown, J.S. and J. Malaika, Effects of particle shape on settling velocity at low Reynolds number, *Trans. Am. Geophys. Un.*, 31(1), 74-82, 1950.

Mishchenko, M.I., Light scattering by size-shape distributions of randomly oriented axially symmetric particles of a size comparable to a wavelength, *Applied Optics*, 32, 4652-4666, 1993.

Murrow, P.J., W.I. Rose, and S. Self, Determination of the total grain size distribution in a vulcanian eruption column, and its implications to stratospheric aerosol perturbation, *Geophys. Res. Let.*, 7 (11), 893-896, 1980.

Neal, C.A., R.G. McGimsey, C.A. Gardner, M.L. Harbin, and C.J. Nye, Tephra-fall deposits from the 1992 eruption of Crater Peak, Mount Spurr, Volcano, Alaska: A preliminary report on distribution, stratigraphy, and composition, *USGS Bull.*, 2139, 65-79, 1995.

Nye, C.J, M.L. Harbin, T.P. Miller, S.E. Swanson, C.A. Neal, Whole-rock major- and trace-element chemistry of 1992 ejecta from Crater Peak, Mount Spurr Volcano, Alaska, *USGS Bull.*, 2139, 119-128, 1995.

Perkins, M. E., Nash, W. P., Brown, F. H., and Fleck, R. J., Fallout tuffs of Trapper Creek

Idaho-A record of Miocene explosive volcanism in the Snake River Plains volcanic province: *Geol. Soc. Am. Bull.*, 107, 1484-1506, 1995.

Pettyjohn, E.S. and E.B. Christiansen, Effect of paticle shape on free-settling rates of isometric particles, *Chem. Eng. Prog.,* 44 (2), 157-172, 1948.

Rawle, A., Basic principles of particle size analysis, *Malvern Instruments Ltd. Technical Papers*, available from the World Wide Web server at http://www.malvern.co.uk, 2000a.

Rawle, A., Malvern sizes up the industry with laser diffraction techniques, *Malvern Instruments Ltd. Laboratory Equiment*, available from the World Wide Web server at http://www.malvern.co.uk, 2000b.

Roller, P.S., Accurate air separator for fine powders, *Industr. Eng. Chem.*, v. 3, 2, 213-216, 1931a.

Roller, P.S., Measurement of particle size with an accurate air analyzer: the fineness and particle size distribution of Portland cement, *U.S. Bureau of Mines Tech. Pap.*, 400, 607-628, 1931b.

Rose, W.I., Scavenging of volcanic aerosol by ash: Atmospheric and volcanologic implications, *Geology*, *5*, 621-624, 1977.

Rose, W.I., A.T. Andersen, L.G. Woodruff, and S.B. Bonis, The October 1974 basaltic tephra from Fuego Volcano: description and history of the magma body, *J. Vol. Geotherm. Res.*, 4, 3-53, 1978.

Rose, W.I., G.J.S. Bluth, D.J. Schneider, G.G.J. Ernst, C.M. Riley, L.J. Henderson, and R.J. McGimsey, Observations of volcanic clouds in their first few days of atmospheric residence: the 1992 eruptions of Crater Peak, Mount Spurr Volcano, Alaska, *J. Geology, 109,* 677-694, 2001.

Rose, W. I., A. B. Kostinski and L. Kelley, Real time C band Radar observations of 1992 eruption clouds from Crater Peak, Mount Spurr Volcano, Alaska, *USGS Bull.*, 2139, 19-28, 1995.

Sarna-Wojcicki, A.M., S. Shipley, R.B. Waitt, D. Dzurisin, and S.H. Wood, Areal distribution, thickness, mass, volume, and grain size of airfall ash from the six major eruptions of 1980, *USGS Prof. Pap. 1250*, 577-600, 1981.

Schmiedel, J., *J. Physik. Z.*, 29, 594-610, 1928.

Schneider, D.J., W.I. Rose, C. Kelley, Tracking of 1992 Eruption Clouds from Crater Peak Vent of Mount Spurr Volcano, Alaska, using AVHR, *USGS Bull.*, 2139, 27-36, 1995.

Schneider, D.J., W.I. Rose, L.R. Coke, G.J.S. Bluth, I.E. Sprod, and A.J. Krueger, Early evolution of a stratospheric volcanic eruption cloud as observed with TOMS and AVHRR, *J. Geophys. Res.*, *104 (D4)*, 4037-4050, 1999.

Sparks, R.S.J., M.I. Bursik, G.J. Ablay, R.M.E. Thomas, and S.N. Carey, Sedimentation of tephra by volcanic plumes. Part 2: controls on thickness and grain-size variations of tephra fall deposits, *Bull. Volcanol.*, 54, 685-695, 1992.

Sparks, R.S.J., M.I. Bursik, S.N. Carey, J.S. Gilbert, L.S. Glaze, H. Sigurdsson, and A.W. Woods, *Volcanic Plumes*, John Wiley and Sons, N.Y., 574 p., 1997.

Stairmand, C.J, Some practical aspects of particle size analysis in industry, 77-87, 1946.

Stringham, G.E., D.B. Simons, and H.P. Guy, The behavior of large particles falling in quiescent liquids, *USGS Prof. Pap. 562-C*, 36 p., 1969.

Swinehart, J.B., V.L. Souders, H.M. DeGraw, R.F. Diffendal, Jr., Cenozoic Paleogeography of Western Nebraska, *Cenozoic Paleogeography of West-central United States*, eds. R.M. Flores and S.S. Kaplan, proceedings of Rocky Mountain Paleogeography Symposium 3, Denver, Colorado, 209-229, 1985.

Suzuki, T., A theoretical model for dispersion of tephra, in, eds. D. Shimozuru and I Yokoyama, Arc Volcanism: Physics and Tectonics, Terra Scientific Pub. Co., Tokyo, 95-113, 1983.

Wadell, H., Sphericity and roundness of rock particles, *J. Geol.*, 86, 443-451, 1932.

Walker, G.P.L., L.Wilson, and E.L.G. Bowell, Explosive volcanic eruptions--I: The rate of fall of pyroclasts, *Geophys. J. R. Astr. Soc.*, 22, 377-383, 1971.

Wen, S. and W.I. Rose, Retrieval of sizes and total masses of particles in volcanic clouds using AVHRR bands 4 and 5, *J. Geophys. Res.*, *99*, 5421-5431, 1994.

Williams, H., F.J. Turner, and C. M. Gilbert, *Petrography: an introduction to the study of rocks in sections*, W.H. Freeman, San Francisco, 72p, 1954.

Wilson, L. and T.C. Huang, The influence of shape on the atmospheric settling velocity of volcanic ash particles, *Earth Plan. Sci. Let.*, *44*, 311-324, 1979.

Zingg, T., Beitrage zur Schotteranalyse, Schweiz, *Mineral. Petrograph. Mitt.*, 15, 39, 1935.

Figure Captions

Figure 1 Examples of irregularly-shaped ash particles. A) Equant mineral grain at left and a small pumice clast at right from the August 1992 Spurr eruption. B) Pumice clasts from the August 1992 Spurr eruption. C) Angular glass bubble-wall shards from the October 14, 1974 Fuego eruption. D) Bubble-wall shards from the Ash Hollow Member ash in Nebraska (Miocene).

Figure 2 Locations of samples used in this study are marked by solid black stars. A) Isopach map of October 14, 1974 Fuego ash deposit (map courtesy of W.I. Rose). B) Isomass map of the ash deposits from the August 1992 Spurr eruption showing a secondary maximum ~150 to 340 km from the volcano (map adapted from Game McGimsey, USGS-AVO). C) Map showing the hypothetical extent of the Miocene Ogallala Formation. The Bruneau-Jarbridge volcanic center may be the source of this ash.

Figure 3 SEM images showing typical particle types (vesicular and nonvesicular) and shapes observed in the ashes studied. A) Vesicular and nonvesicular basaltic clasts in Fuego ash. B) Vesicular pumice clasts and nonvesicular glass shards in andesitic ash from Spurr. C) Bubble-wall shards from the rhyolitic ash of the Ash Hollow Member, NE.

Figure 4 Grain size distributions determined by laser diffraction. A) The Fuego , B) Spurr and C) Ash Hollow member ash samples are all sedimentologically poorly-sorted and rich in fines. The Spurr sample has a distint bimodal distribution. Grain size values below 10 microns become increasingly inaccurate with decreasing size due to limitations in the laser diffraction method.

Figure 5 Shape and size parameters compared with terminal velocity for all three ash compositions. Values are combined means (measurements for both pumice and glass particle types are used). A) Error bars show the standard deviation of the combined mean and would have similar relative values in other shape and size parameter graphs. The feret averages for Fuego and Spurr are similar, but Ash Hollow (NE) ash has a different pattern. B) Aspect ratios for all ashes differ greatly from the value (1.0) typically assumed for spherical particles. See Table 1 for definitions of the different shape and size parameters.

Figure 6 Comparison of measured terminal velocities to terminal velocities calculated for spheres of the appropriate densities (1.5, 1.7, 2.1, 2.3 g/cm^3 for Spurr, 2.4 and 2.6 g/cm^3 for Fuego, and 2.3 g/cm^3 for Ash Hollow). Values are combined means. All diameter measurements except 'inner diameter' are much larger than diameter values predicted for spherical particles at the same terminal velocities. See Table 1 for definitions of the different diameter measurements.

Figure 7 Shape and size parameters compared to terminal velocity for the combined, vesicular, and nonvesicular mean values of particles in Fuego ash. Density curves for spherical particles are plotted for feret average to assess density influences on terminal velocity. A) Feret average shows that most vesicular particles have larger values than nonvesicular particles at similar terminal velocities. B) Aspect ratio shows that nonvesicular particles have higher values than vesicular particles at similar terminal velocities.

Figure 8 Shape and size parameters compared to terminal velocity for the combined, vesicular, and nonvesicular mean values of particles in Spurr ash. The arrow in A) denotes the TV = 21.5 cm/s peak found in some diagrams (see text). The vertical dashed line in B) marks the change in shape parameter values which may be related to changes in fragmentation mechanisms.

Figure 9 BET (Brunauer, Emmett, and Teller method) surface area compared to calculated surface area for various geometrical shapes. Calculated surface areas were derived using image analysis measurements for radius (r), width (w), length (l), and thickness (t) (for cylinders r=feret average, l=length; for ellipse l=length, w=width, r=feret average; for sphere r=feret average; for disk t= 20 μm, r=feret average) and total grain size distributions of the deposits. The dashed line represents equal values of calculated surface area and measured surface area (1:1 ratio).

Figure 10 Measured perimeter compared to the calculated perimeter of spheres that would fall out at the same settling velocity. Dotted lines represent ratios of calculated perimeters to measured perimeters.

Figure 11 Surface area compared to perimeter for various geometrical shapes. All calculated values of Surface area and perimeter were derived using the image analysis measurements of feret average, width, and length. The dotted lines represent ratios of BET/calculated surface areas to measured/calculated perimeters.

Figure 12 Feret diameter compared to the calculated diameter of spheres that would fall out at the same settling velocity.

Appendix Figures

Figure A1 Laser diffraction method used in the Mastersizer instrument to relate the amount of light scattered by the particle to a particle diameter. Small particles produce large angles of scattering while large particles produce small angles of scattering.

Figure B1 Diagram showing the Roller particle size analyzer. Important parts of the instrument are labeled and the sorting method is described in the text.

Figure D1 Aggregates formed during sorting in the Roller analyzer. Photomicrographs of A) Basaltic ash from the October 14, 1974 eruption of Fuego and B) Rhyolitic ash from the Ash Hollow Member (Miocene). C) SEM backscatter image of Andesitic ash from the August 18, 1992 eruption of Mount Spurr.

Figure E1 Preparation of the ash sample for imaging. The ash sample is transported through the plastic tube to the aluminum stub to adequately separate and randomly orient the ash particles for image analysis.

Figure F1 Image analysis of the sample. An SEM image is taken of the ash particles and a bit-map (inset) is made of the image (blue color). Frames (blue and red) are used to identify the particles to be measured by the image analysis program. Particles outside the selection box are omitted. Particles less than 10 X 10 pixels are selected or “trapped” and removed from further analysis. Particles are measured automatically and then checked by hand (outlined particle) to ensure that the image analysis program has outlined the particle correctly.

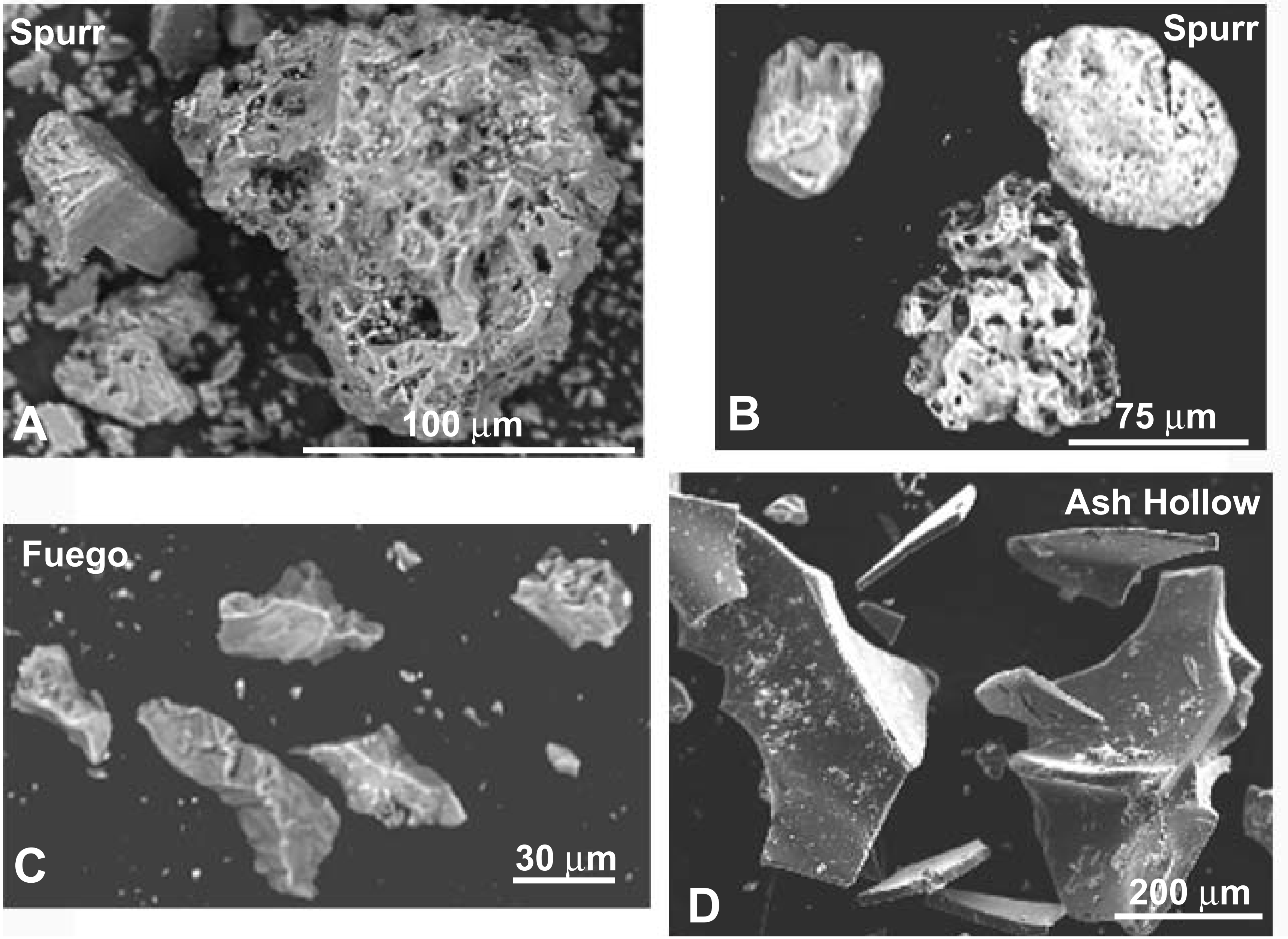

Spurr
A
100 μm
Spurr
B
75 μm
Fuego
C
30 μm
Ash Hollow
D
200 μm

Riley et al. Figure 2

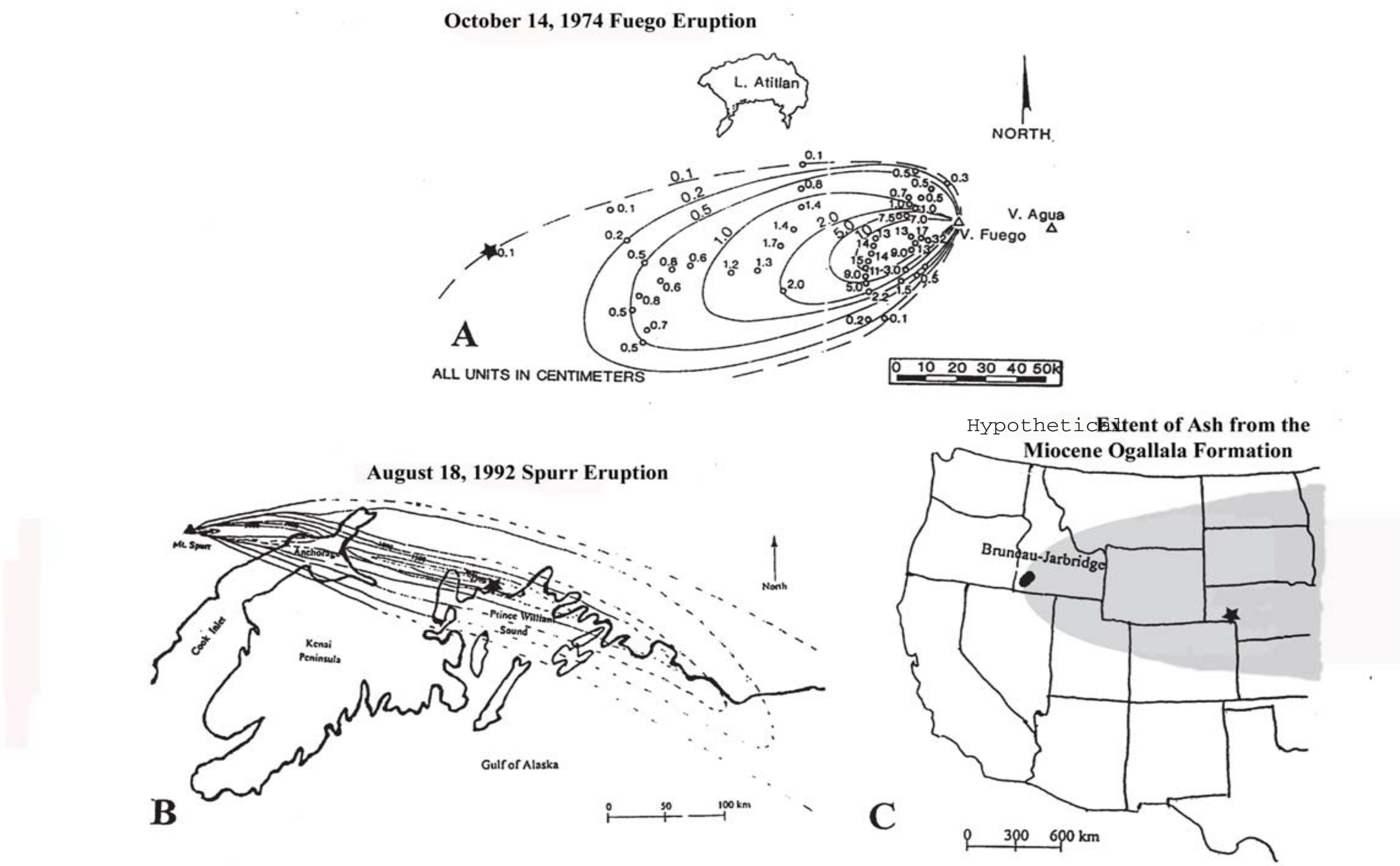

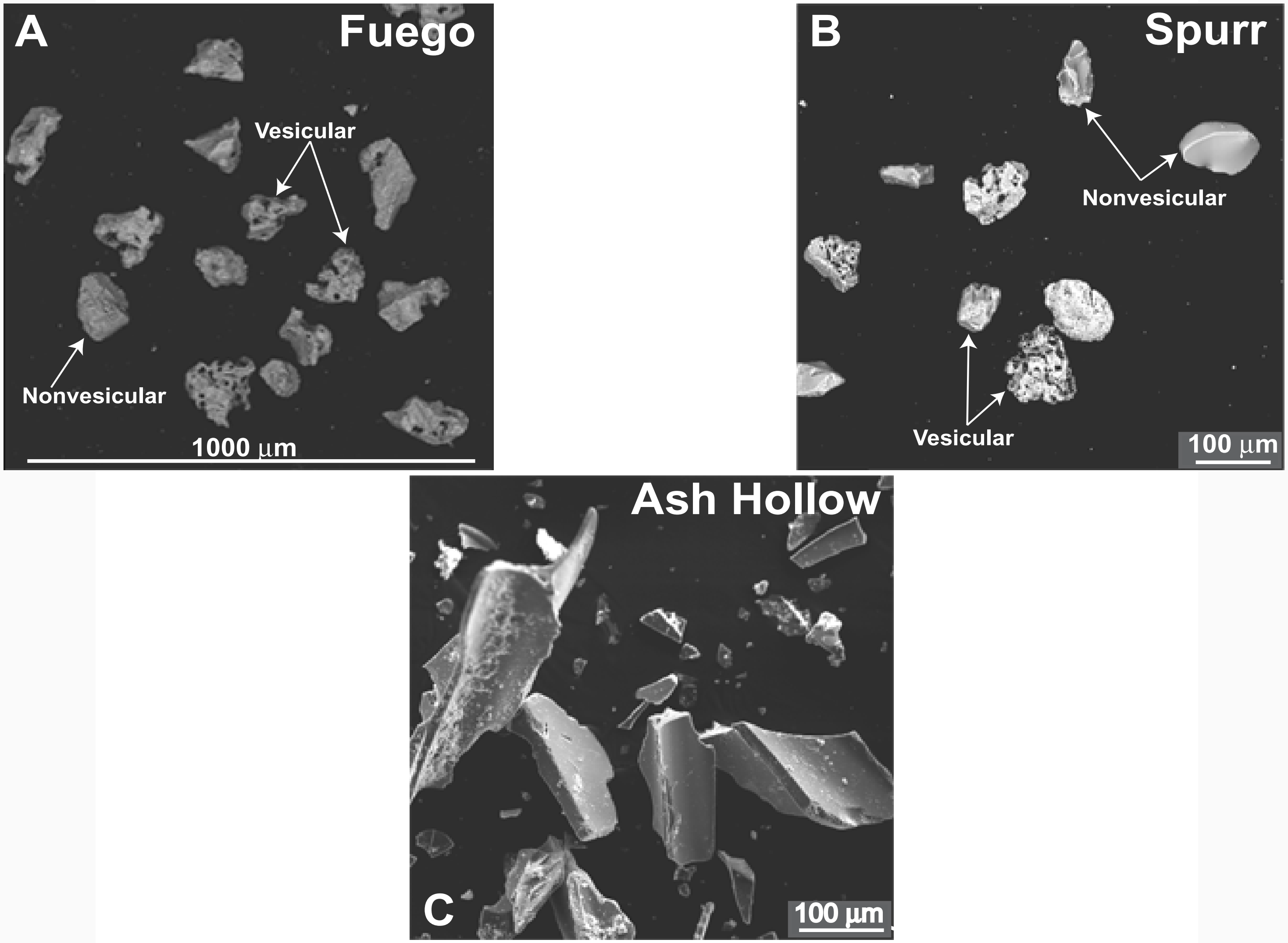
A
Fuego
Vesicular
Nonvesicular
1000 µm
B
Spurr
Nonvesicular
Vesicular
100 µm
Ash Hollow
C
100 µm

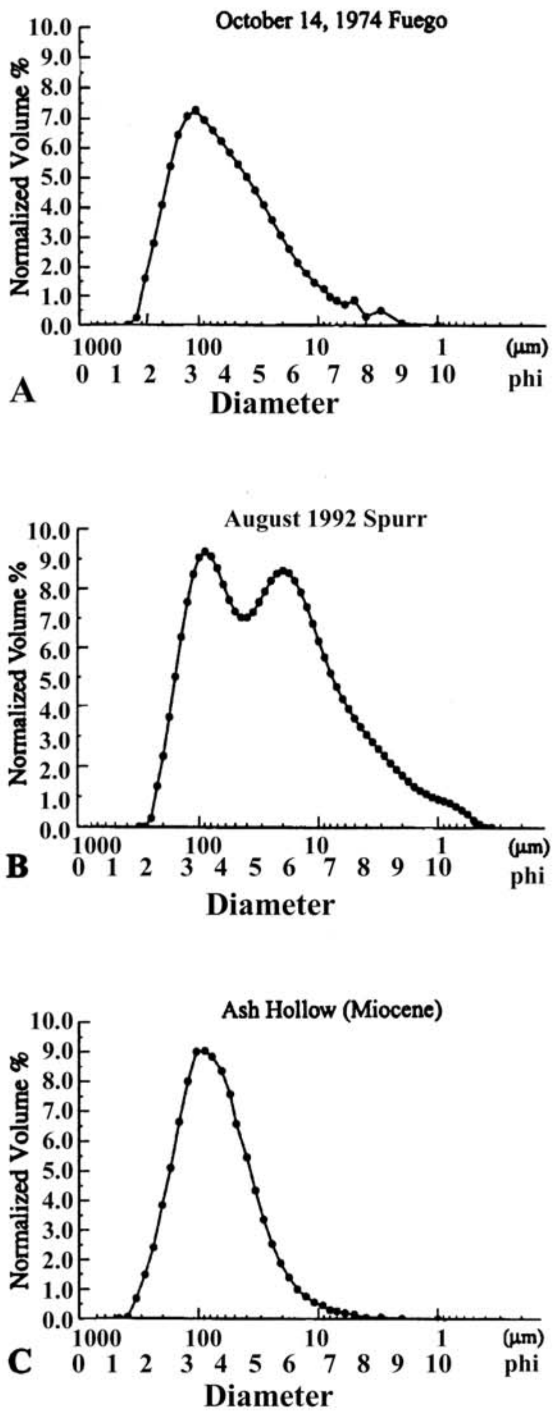
October 14, 1974 Fuego
Normalized Volume %
10.0
9.0
8.0
7.0
6.0
5.0
4.0
3.0
2.0
1.0
0.0
1000 100 10 1 (µm)
0 1 2 3 4 5 6 7 8 9 10 phi
A
Diameter
August 1992 Spurr
Normalized Volume %
1000 100 10 1 (µm)
0 1 2 3 4 5 6 7 8 9 10 phi
B
Diameter
Ash Hollow (Miocene)
Normalized Volume %
1000 100 10 1 (µm)
0 1 2 3 4 5 6 7 8 9 10 phi
C
Diameter

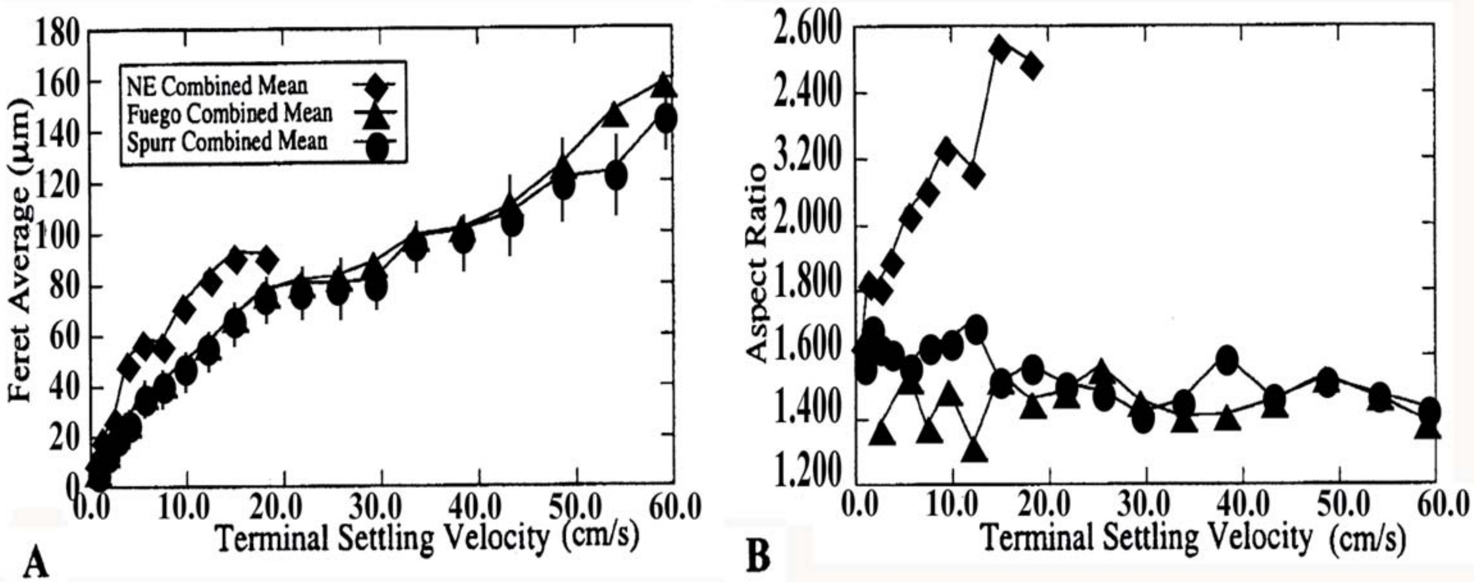

180
160
140
120
100
80
60
40
20
0
Feret Average (μm)
NE Combined Mean
Fuego Combined Mean
Spurr Combined Mean
0.0
10.0
20.0
30.0
40.0
50.0
60.0
Terminal Settling Velocity (cm/s)
A
2.600
2.400
3.200
2.000
1.800
1.600
1.400
1.200
Aspect Ratio
0.0
10.0
20.0
30.0
40.0
50.0
60.0
Terminal Settling Velocity (cm/s)
B

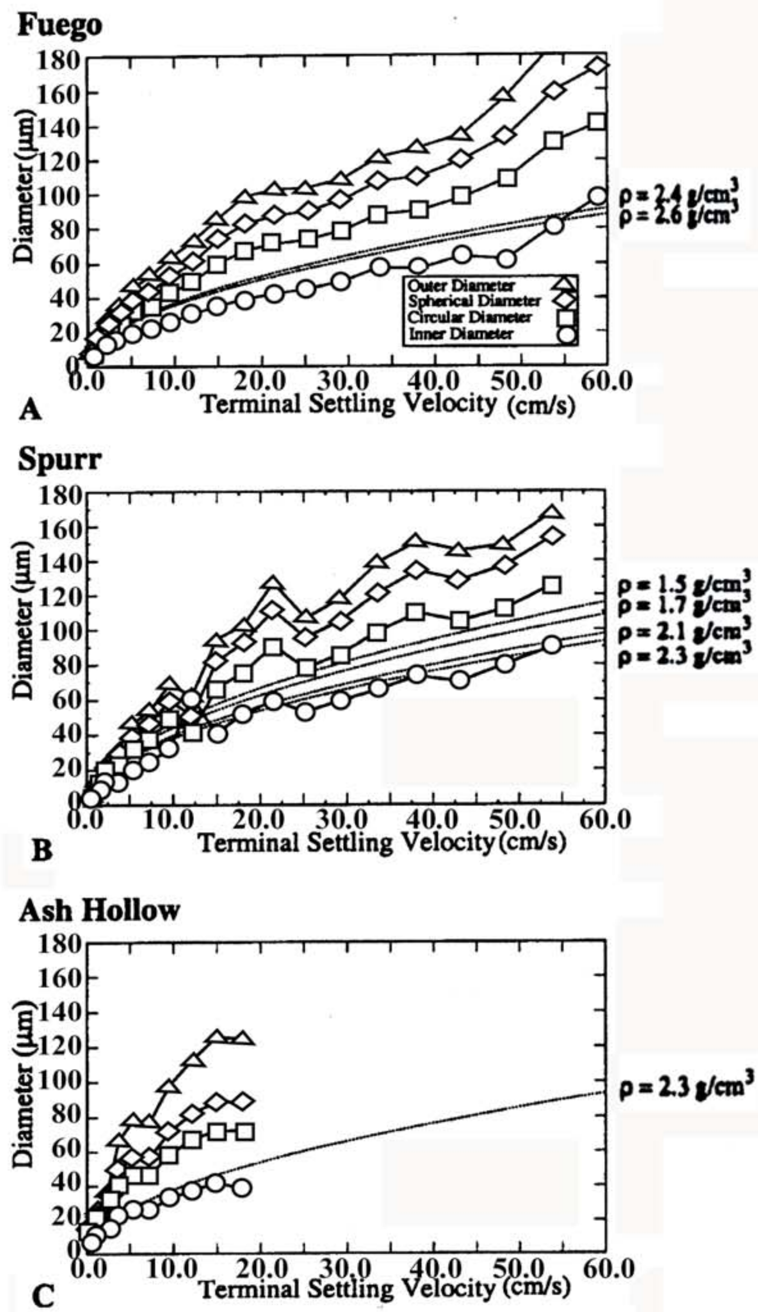
Fuego
Diameter (μm)
Terminal Settling Velocity (cm/s)
ρ = 2.4 g/cm³
ρ = 2.6 g/cm³
Outer Diameter
Spherical Diameter
Circular Diameter
Inner Diameter
A
Spurr
ρ = 1.5 g/cm³
ρ = 1.7 g/cm³
ρ = 2.1 g/cm³
ρ = 2.3 g/cm³
B
Ash Hollow
ρ = 2.3 g/cm³
C

Riley et al. Figure 7

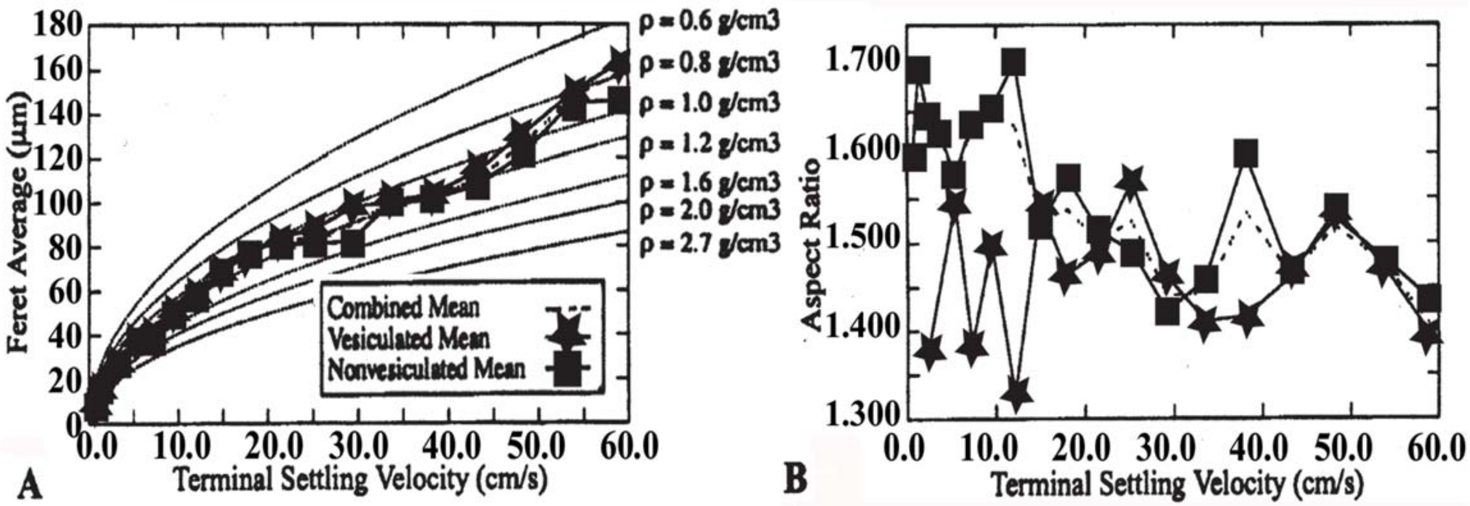

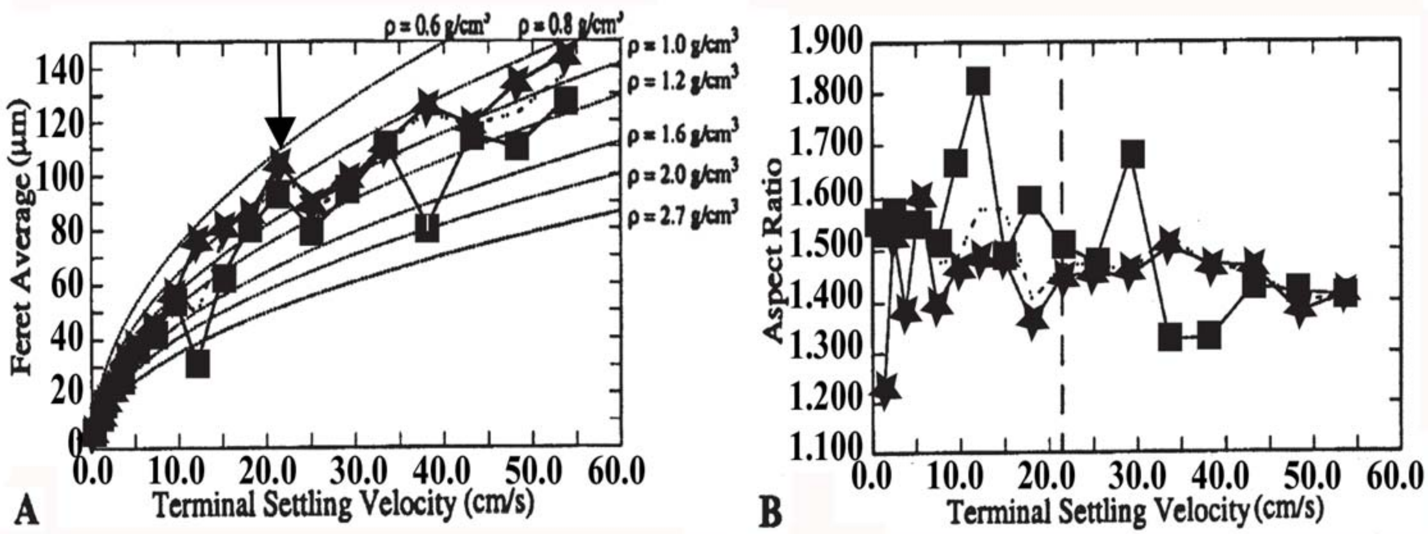
ρ = 0.6 g/cm³
ρ = 0.8 g/cm³
ρ = 1.0 g/cm³
ρ = 1.2 g/cm³
ρ = 1.6 g/cm³
ρ = 2.0 g/cm³
ρ = 2.7 g/cm³
Feret Average (μm)
Terminal Settling Velocity (cm/s)
A
Aspect Ratio
Terminal Settling Velocity (cm/s)
B

Riley et al. Figure 9

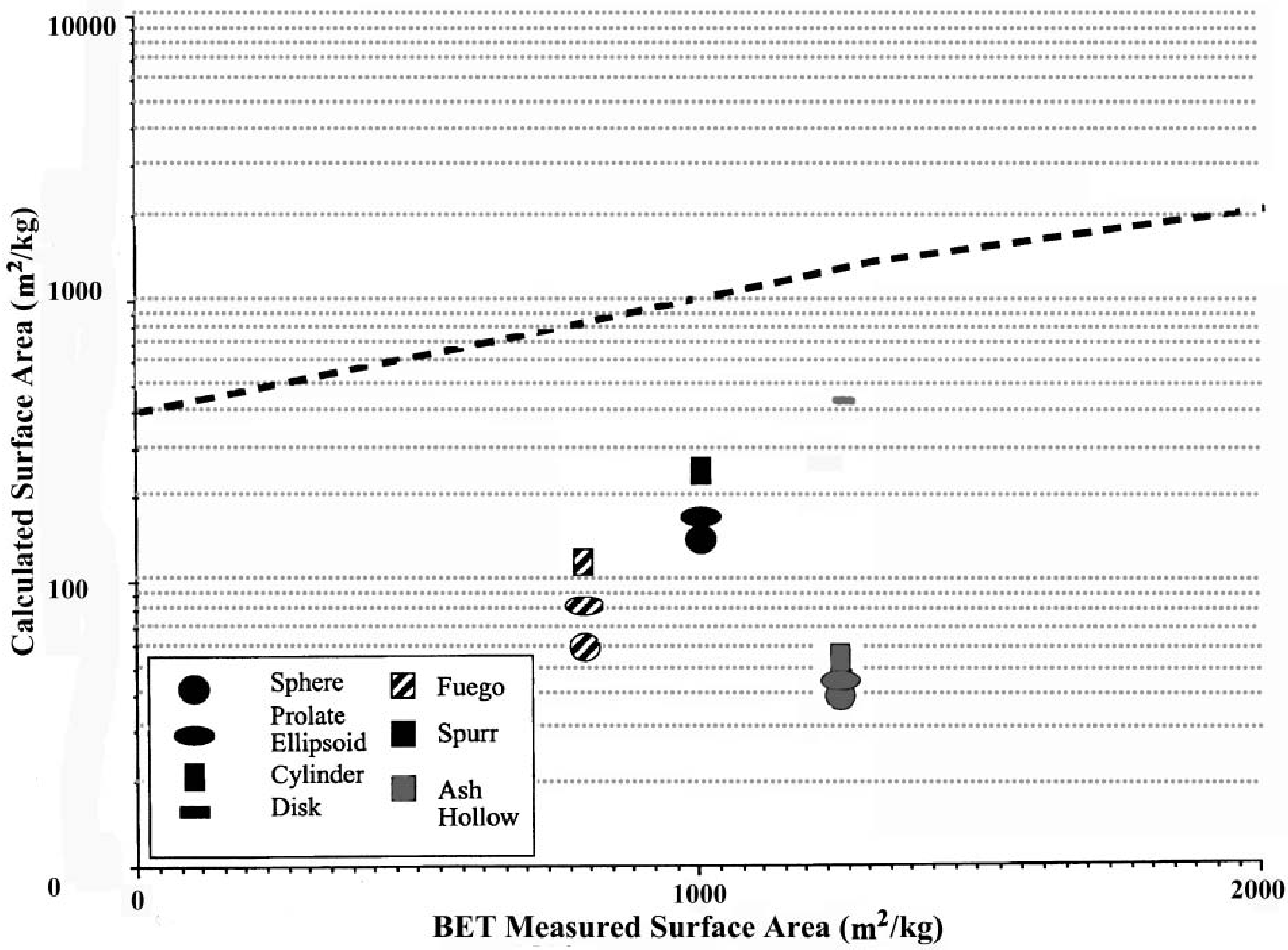

Riley et al. Figure 10

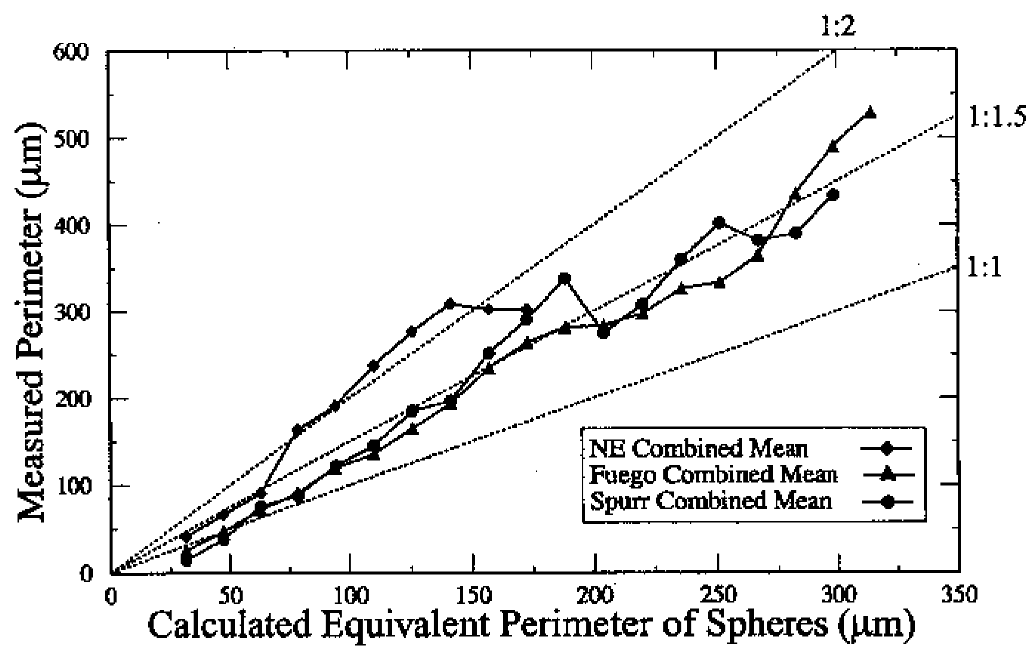

Riley et al. Figure 11

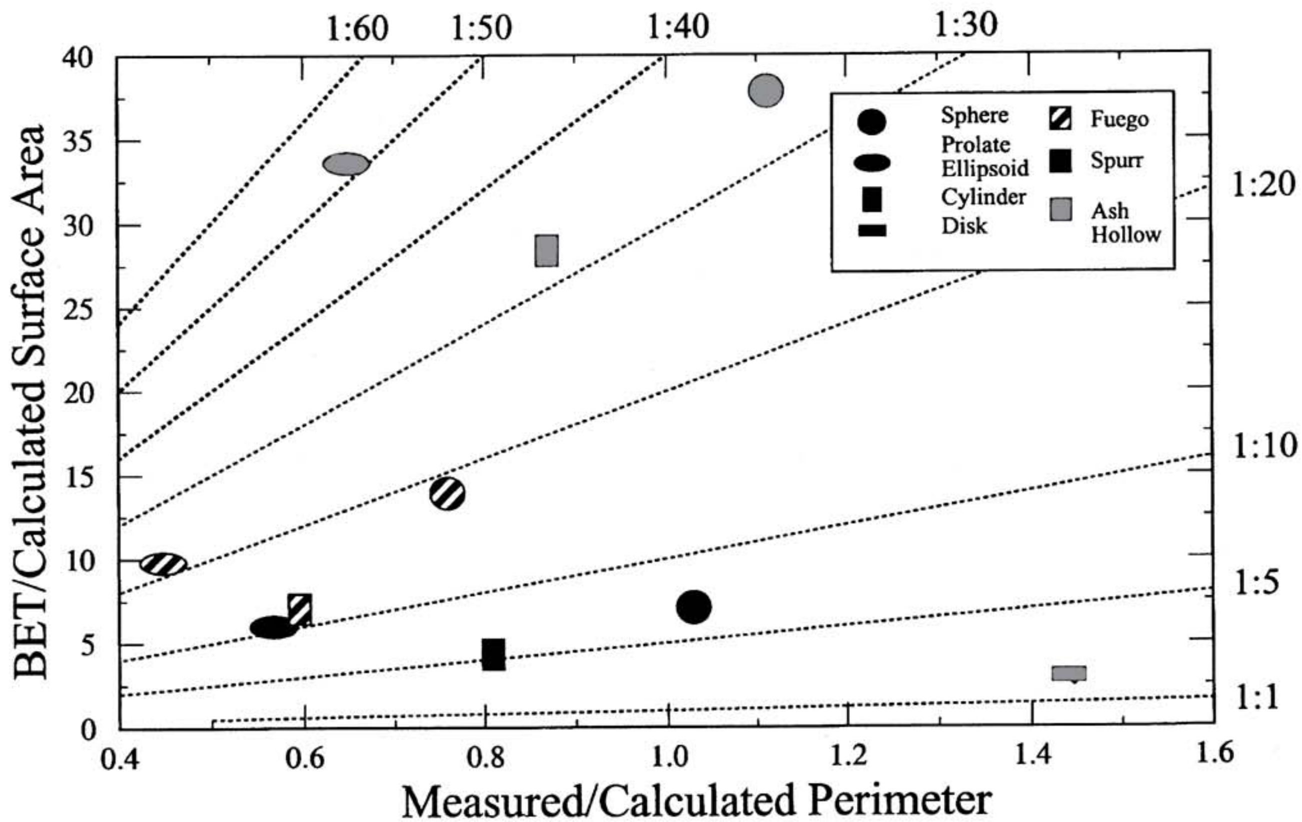

Table 1. Image Analysis Measurement Definitions

Shape and Size Parameters	*Definition*
Area (μm^2)	Sum of pixels in an object.
Filled Area (μm^2)	Sum of pixels in an object including holes.
Perimeter (μm)	Sum of pixels making up the object boundary.
Convex Perimeter (μm) 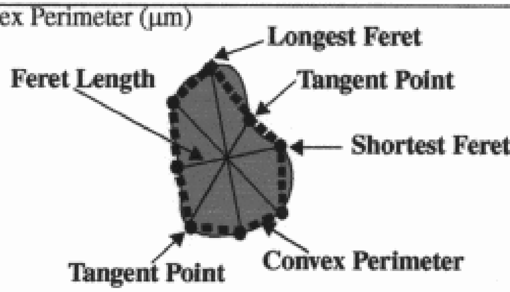	Estimates convex perimeter by adding the pixels making up straight-line distances between feret tangent points along a particle's perimeter. ***Feret*** length is the distance between two parallel tangents on opposite sides of an object measured at specific angles (see graphic for an example). In this study, 64 ferets were measured for each particle at angles of 5.6° Σ (feret)(2tan[π/2(number of ferets)])
Length (μm)	Longest of 64 ferets measured for an object (see graphic above).
Width (μm)	Shortest of 64 ferets measured for an object (see graphic above).
Aspect Ratio (dimensionless)	Length/Width
Roughness (dimensionless)	Convex Perimeter/Perimeter
Compactness (dimensionless)	4πArea/Convex Perimeter^2
Sphericity (dimensionless)	4πArea/Perimeter^2
Feret Average (μm) 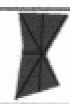	Average length of 64 feret measurements.
Inner Diameter (μm) 	Diameter of the largest circle that can fit completely within an object.
Outer Diameter (μm) 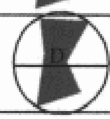	Diameter of the smallest circle into which objects can fit completely.
Spherical Diameter (μm)	Estimates the diameter of an equivalent sphere (3-D object). $2\,(1.2247)(\text{area}/\pi)^{1/2}$
Circular Diameter (μm) 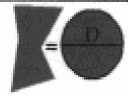	Estimates the diameter of an equivalent a circle (2-D object). $2\,(\text{area}/\pi)^{1/2}$
String Length (μm)	Longest measure of diameter assuming object is thin, curved, and elongate. $(\text{Perimeter} + (\text{Perimeter}^2\text{-}16(\text{Area}))^{1/2})/4$
String Width (μm)	Shortest measure of diameter assuming object is thin, curved, and elongate. $(\text{Perimeter} - (\text{Perimeter}^2\text{-}16(\text{Area}))^{1/2})/4$
X-Projection (μm) 	Sum of pixels between the vertical intercepts of a particle divided by 2.
Y-Projection (μm) 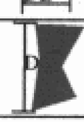	Sum of pixels between the horizontal intercepts of a particle divided by 2.

Table 2. Grain Size Characteristics of Ash Samples

Sample	Mdϕ (ϕ)	Mdϕ (μm)	σ_ϕ	α_ϕ
Fuego	4.9	33.5	1.34	+1.05
Spurr	5.3	25.0	1.78	+0.42
Ash Hollow	3.7	76.9	1.07	+0.38

Table 3. Summary of Selected Shape Data

	Fuego	Spurr	Ash Hollow
TV = 1.3 cm/s			
Feret Average (µm)	15	12	21
Aspect Ratio	1.7	1.5	1.8
Perimeter (µm)	47	38	66
Convex Perimeter (µm)	45	36	65
TV = 7.3 cm/s			
Feret Average (µm)	40	45	60
Aspect Ratio	1.6	1.5	2.1
Perimeter (µm)	135	145	240
Convex Perimeter (µm)	130	140	180
TV = 18.0 cm/s			
Feret Average (µm)	80	90	90
Aspect Ratio	1.5	1.4	2.5
Perimeter (µm)	265	290	300
Convex Perimeter (µm)	245	280	290
TV = 43.1 cm/s			
Feret Average (µm)	110	120	
Aspect Ratio	1.5	1.5	
Perimeter (µm)	365	380	
Convex Perimeter (µm)	345	370	
BET Surface Area (m^2/g)	0.7919	1.0059	1.2291
Calc. Surface Area[a] (m^2/g)	0.06	0.14	0.03

a. Calculated using surface area equation for a sphere and feret diameter.

Table 4. Calculated Surface Areas Using Correction Factors and Different Grain Size Distribution Determinations

	Surface Area Correction Factor[a] (F)	BET Surface Area (m^2/g)	Corrected[b] Laser Diffraction Surface Area (m^2/g)	Corrected[b] Sieve and Coulter Counter Surface Area (m^2/g)
Fuego	14	0.7919	1.0	1.9
Spurr	7	1.0059	1.6	na
Ash Hollow	38	1.2291	1.7	na

a. F = BET surface area divided by calculated surface area from grain size data

b. Calculated surface area from grain size data multiplied by the correction factor

Appendix A: Determining Grain Size Distributions Using Laser Diffraction

Grain size distributions for the bulk ash samples were measured using laser diffraction analysis. Subsamples of less than 1g were taken from the ash samples using standard powder-handling techniques so that representative samples were obtained, and then run through the Malvern Mastersizer 2000 laser diffraction instrument. The Mastersizer is capable of fine particle measurements of < 1 µm diameter to 2000 µm, although data below 10 µm diameter becomes increasingly unreliable. Measurements are obtained by transporting the ash particles through a water-filled tube past a red and blue laser beam (Figure A1; Rawle 2000a and 2000b). When the laser beam encounters a particle the beam is diffracted and light is scattered at various angles and detected by a photodetector array. The light intensity depends on the scattering angle; laser diffraction by larger particles will produce low angles of scattering while diffraction by smaller particles will produce high angles of scattering (Figure A1). The Malvern instrument uses Mie theory to relate the amount of light energy detected to a spherical particle diameter (Malvern Instruments Ltd., 2000; Rawle, 2000b. The particle refractive index used by the instrument for all ash samples was 1.53 and the dispersant refractive index was 1.33. Samples were run through the Mastersizer twice to obtain accurate results.

Appendix B: Sorting the Ash Samples Using the Roller Particle Size Analyzer

The Roller particle size analyzer (Figure B1) has been used in industry for decades to sort materials such as cement and is considered a highly accurate particle separation device (Roller, 1931a; 1931b; Stairmand et al., 1946). Silica microspheres (1-100 microns in diameter) were used to test the instrument, and the microspheres were accurately sorted into the appropriate terminal velocity groups as determined for spherical particles in a laminar flow regime.

For the ashes, approximately 10-20 grams of the original samples were placed into the glass goose-neck intake tube of the instrument (Figure B1). Filtered air was then blown into the glass intake tube through a specific-sized nozzle (Table B1) and the sample was elutriated into a settling chamber. The settling chamber is shaken by a rotary tapper to prevent sample adhesion to the chamber walls. Laminar flow carries the particles from the base of a three foot chamber to the top of the chamber and into a glass goose-neck outtake tube where the sample is deposited in a fiber collection thimble that is lined with wax paper. Airflow rates are adjusted using a flowmeter, different diameter settling chambers, and different nozzle sizes (Table B1) to suspend spherical particles of specific diameters.

To begin sorting the ash sample, a settling chamber and nozzle size were chosen (Table B1) so that the lowest terminal velocity particles were collected, then, progressively higher terminal velocity particles were collected with each consecutive run. Airflow rate was adjusted and allowed to run for two minutes before attaching a collection thimble to the outtake tube and engaging the rotary tapper allowing the smaller ash particles to fill the settling chamber. The length of the run (Table B1) is based on fly ash experiments (American Instrument Company Roller analyzer manual at Michigan Technological University) and is longer than the minimum time to suspend all the particles in the specific terminal velocity group. If the run time is too long, particles with higher terminal velocities were suspended because the settling chamber walls creating friction and causing a nonuniform velocity field to develop (Roller, 1931a). After the designated run time, airflow was stopped and the collection thimble removed. The glass outtake tube was washed to prevent contamination between sorted groups. The procedure was repeated for the next sorted group using a new collection thimble.

Appendix C: The Relationship of Terminal Velocity to Flow Rate

Different flow rates were used for the Roller analyzer to sort the ash sample into terminal velocity groups. Flow through the Roller analyzer is laminar. Reynold's number calculations show that a laminar flow regime is appropriate for fine volcanic ash (< 62.5 microns) falling out of a volcanic cloud (Bonadonna et al., 1998). The appropriate Stoke's law equation governing laminar particle fall is:

V = [gd^2(p-s)]/[18n] Equation C1

where V is terminal velocity, g is the gravitational acceleration (980 cm/s^2), d is the spherical particle diameter, p is the density of the particle, s is the density of the fluid medium (0.0012 g/cm^3 for air at sea level and room temperature), and n is the viscosity of the fluid medium (1.82 x 10-4 poise for air at sea level and room temperature). Since the density of air is three orders of magnitude smaller than the particle density, it can be neglected. The above values are substituted and the equation becomes:

V = 29.91 x 10^4 pd^2 (cm/s). Equation C2

Several flow rates (10-18) were selected to sort the ash samples into groups. The flow rates were related to terminal velocity by incorporating an equation for flow rate into the Stoke's law equation (equation C2). The flow

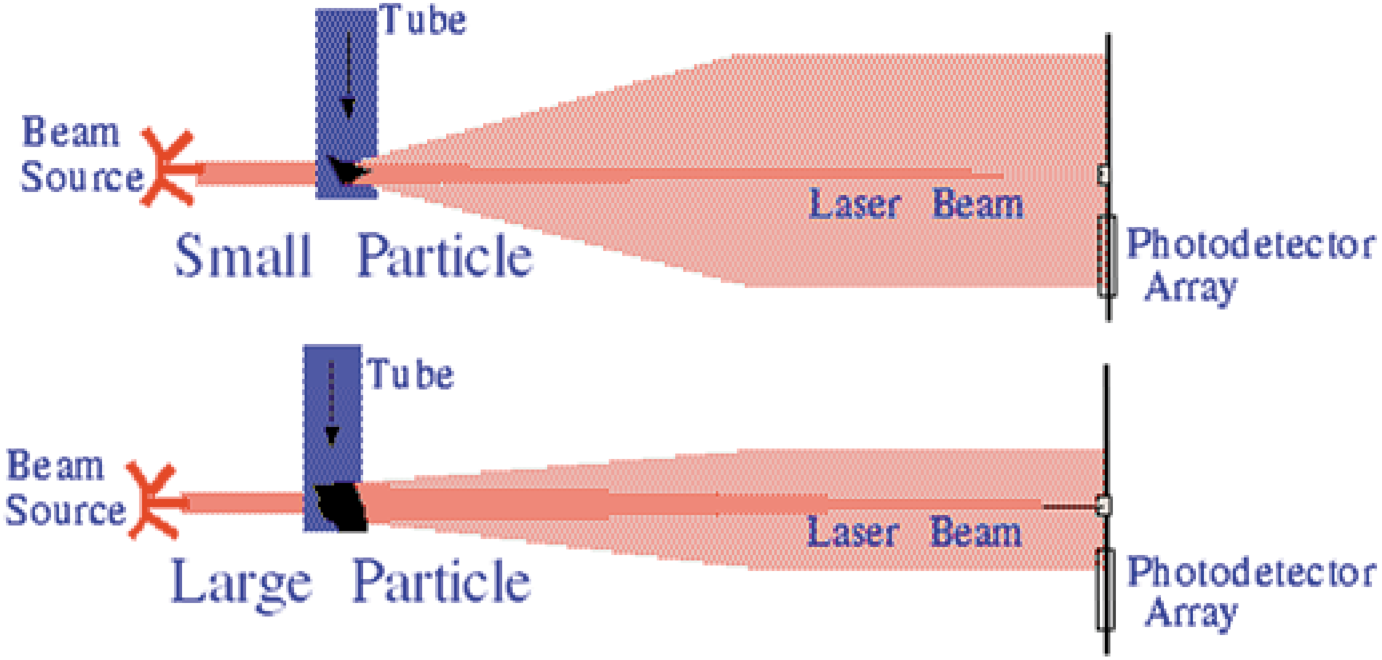
Tube
Beam
Source
Laser Beam
Small Particle
Photodetector
Array
Tube
Beam
Source
Laser Beam
Large Particle
Photodetector
Array

Riley et al.   Figure B1

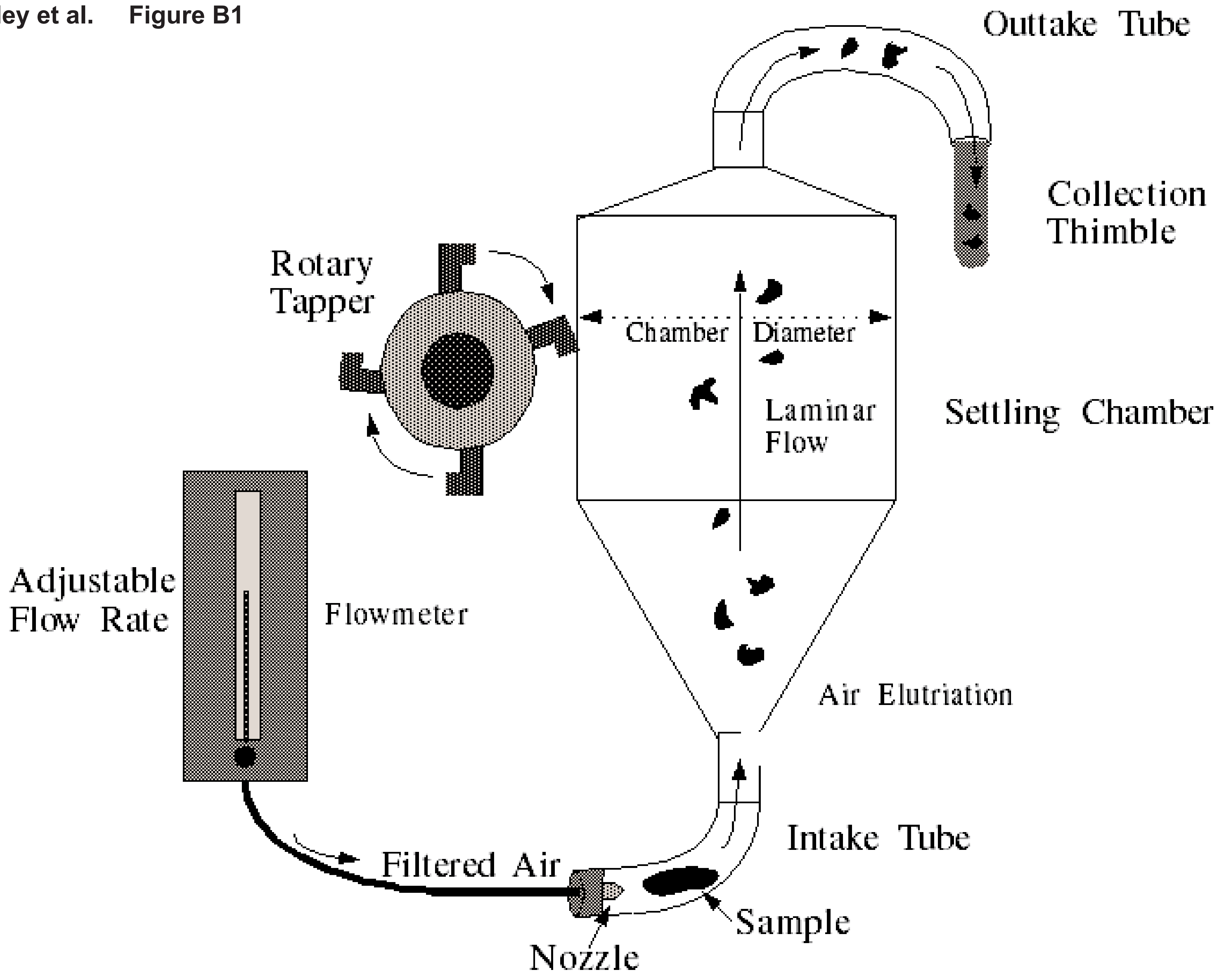

Table B1: Roller Analyzer Flow Rates

Terminal Velocity (cm/s)	Equivalent[a] Spherical Particle Size Suspended (μm)	Flow Rate (l/min)	Settling Chamber Diameter (cm)	Nozzle Size (cm)	Run Time (min)
0.6	10	14.7	22.9	.208	25
1.3	15	8.3	11.4	.150	30
2.4	20	14.7	11.4	.208	20
3.7	25	22.9	11.4	.244	15
5.4	30	8.3	5.7	.150	20
7.3	35	11.3	5.7	.178	15
9.5	40	14.7	5.7	.208	15
12.2	45	18.6	5.7	.226	10
14.9	50	23.0	5.7	.244	10
18.0	55	8.6	3.2	.150	15
21.5	60	10.2	3.2	.178	15
25.2	65	12.0	3.2	.178	15
29.2	70	13.9	3.2	.208	10
33.5	75	15.9	3.2	.226	10
38.1	80	18.1	3.2	.226	10
43.1	85	20.5	3.2	.244	10
48.3	90	23.0	3.2	.244	10
53.8	95	25.5	3.2	.244	10
59.0	>95	sample remaining in intake tube			

a. Calculated for spheres of density 2.7 g/cm^3.

rate, F, is equal to the terminal velocity multiplied by the cross-sectional area of the settling chamber:

$$F = V ((\pi D^2)/4) \quad (cm^3/s) \qquad \text{Equation C3}$$

where D is the diameter of the settling chamber (cm). By substituting for V in Equation C3 and using Equation C2, we get:

$$F = 0.1409 \times 10^{-3} p d^2 D^2 \quad (l/min) \qquad \text{Equation C4}$$

where p is the density of ash (which varies between ~2.3 to >3.0 g/cm^3 depending on the sample material).

Silicate microspheres (0-100 microns) with a density of 2.7 g/cm^3 were run through the Roller analyzer to verify that the calculated flow rates correctly estimated terminal velocity within the chamber.

Appendix D: Aggregate Formation in the Roller Analyzer

Incorrect determinations of terminal velocity by the Roller analyzer for individual particles are possible if ash particles are electrostatically charged and clump together in the settling chamber to form aggregates. To determine if there was any particle aggregation during our experiments, the settling chamber was sampled after each sorting run of the volcanic ashes. The intake tube was removed from the bottom of the chamber and a thin section slide was held in its place. The chamber was then tapped until ash fell onto the thin section slide, thus providing a sample of ash that was elutriated into the settling chamber at different flow rates.

The thin section slides (Figure D1) showed that for the Fuego ash, low terminal velocity groups (0.6-2.4 cm/s) contained aggregated clumps averaging 230 microns in diameter. For the Spurr ash, terminal velocity groups (0.6-3.7 cm/s) had aggregates averaging 250 microns in diameter. For the Ash Hollow sample, only the lowest terminal velocity group (0.6 cm/s) had aggregates (average diameter ~190 microns). All aggregates were composed of hundreds of interlocking particles (average diameter 20-30 microns). The terminal velocities which contained aggregates also coated the walls of the collection thimbles (unlike the other settling groups which showed ash accumulation only in the bottom of the thimble).

Appendix E: Sample Preparation for Imaging

Between 0.4-0.5 g of the ash sampled for each terminal velocity group was applied to aluminum stubs for use with the scanning electron microscope (Figure E1). The subsamples were first decharged with a zerostat gun to prevent electrostatic clumping, then dropped into a fast moving, turbulent air stream through a plastic tube and deposited in random orientations onto a carbon sticky tab on the surface of the aluminum stubs. The stub distance from the end of the plastic tube is determined by trial and error so that particles are adequately separated. Separation between particles is necessary to obtain shape measurements for individual particles using an automated image analysis program.

Appendix F: Image Analysis Techniques

Image analysis was done using backscattered electron images of particles in each terminal velocity group for each ash sample. Secondary electron images were not used because resultant cracking of the carbon sticky tab on the aluminum stubs produced visible patterns that led to inaccurate shape measurements using the automated image analysis program. Higher condenser lens settings were used for slow settling particle groups because the electron beam was too strong at lower condenser lens settings, causing the carbon sticky tabs to melt and particles to move.

Image magnification was chosen to allow for the optimum particle separation and resolution. Both fine and coarse particles were imaged if they were observed in the same terminal velocity group, but only the coarser particles were systematically examined for shape characterization.

The contrast between the dark carbon background and light colored ash particles allowed bit maps to be made of the particles in each image (Figure F1). Bit maps were used to highlight pixels in the ash particles. In some terminal velocity groups, both large and small particles were imaged and a function which removes clusters of pixels less than a specified size (typically less than 10 X 10 pixels) was used to get rid of particles judged to be too small for the program to distinguish shape. The 10 X 10 pixel limit was chosen because shape measurements for these particles had sphericity values equivalent to that of a perfect sphere even though they were not spherical. After measurements were obtained, particles were individually selected to verify whether the computer properly outlined particles and to ensure that particles were separated from each other.

Appendix G: BET Surface Area Measurements

The BET (Brunauer, Emmett, and Teller) method is commonly used on powders to obtain reliable surface area measurements (< 10% error) and was used to determine the surface areas for bulk samples of all three ashes

(Brunauer, 1945). This technique injects liquid nitrogen into a container holding the ash sample and assumes that the gas adsorbs onto the powder in multiple uniform layers. Pressure is decreased over time and the volume of gas for each pressure change is plotted to obtain an isotherm. The isotherm represents the point at which an equal amount of gas is being absorbed and released. The intercept of the isotherm provides the volume of gas absorbed onto the sample. Surface area can be calculated by knowing the gas molecule size and number of molecules in the measured volume of gas.

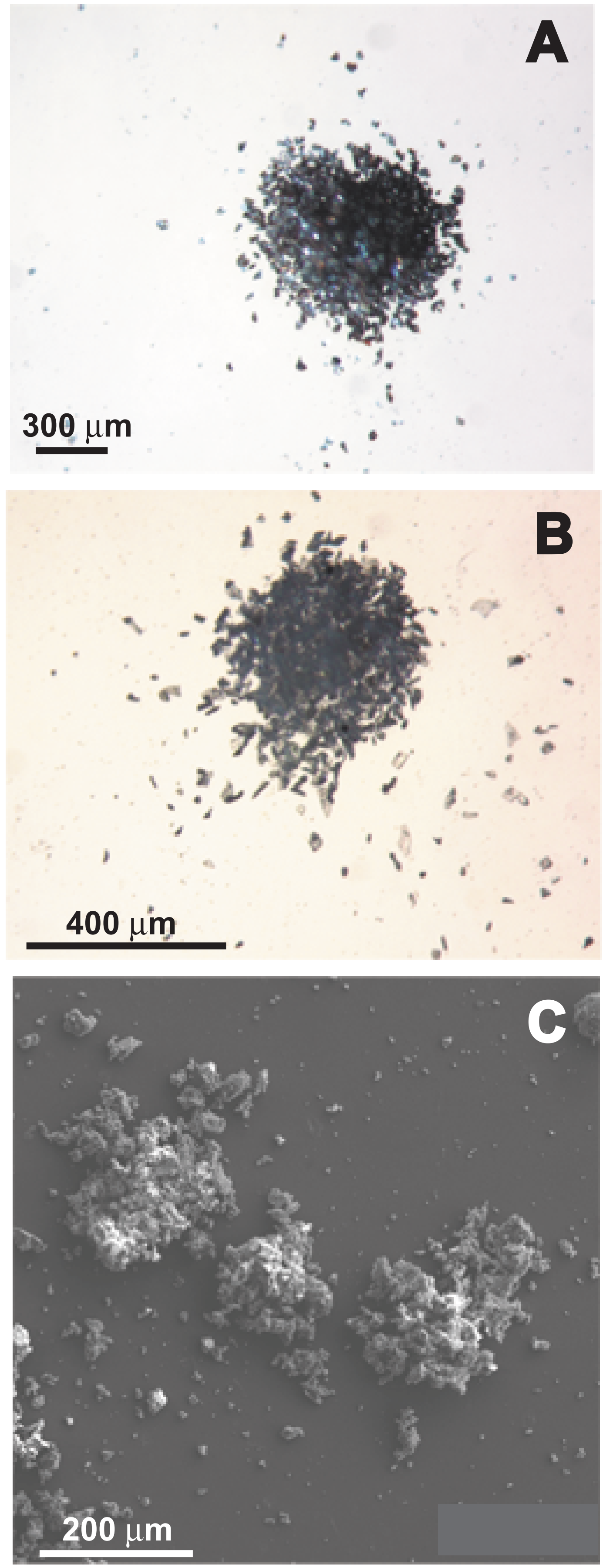
A
300 μm
B
400 μm
C
200 μm

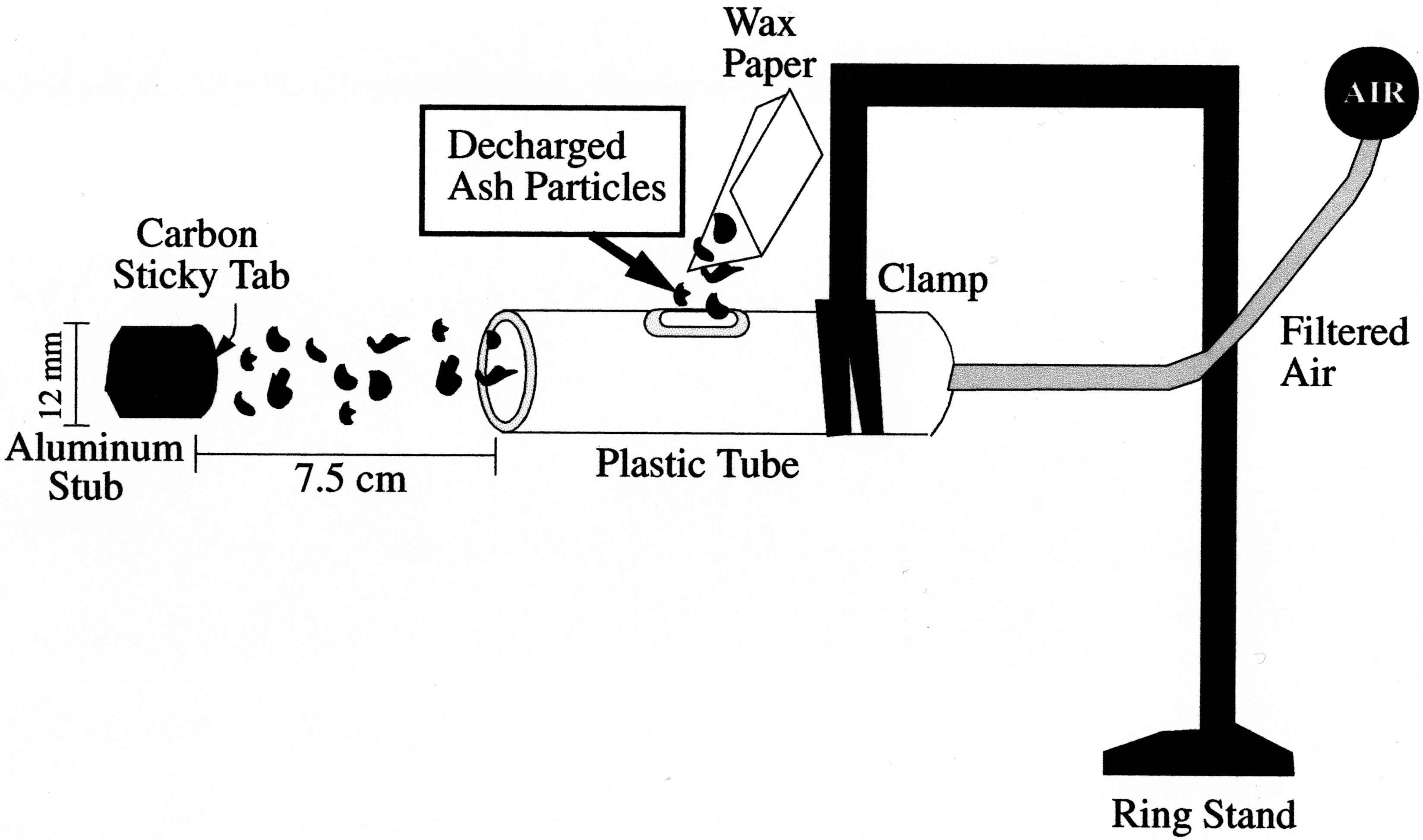
Wax
Paper
Decharged
Ash Particles
Carbon
Sticky Tab
12 mm
Aluminum
Stub
7.5 cm
Plastic Tube
Clamp
AIR
Filtered
Air
Ring Stand

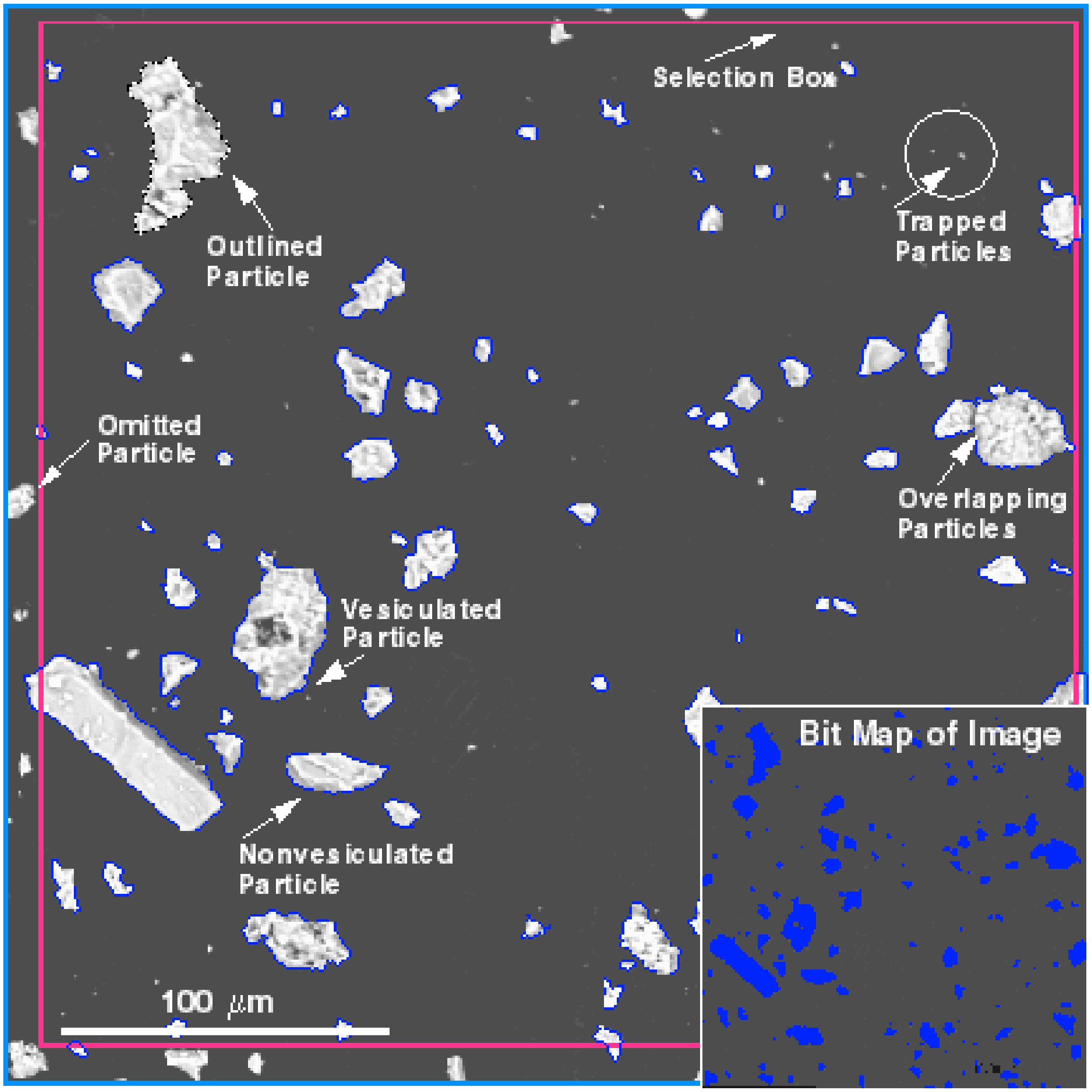
Selection Box
Trapped Particles
Outlined Particle
Omitted Particle
Overlapping Particles
Vesiculated Particle
Nonvesiculated Particle
100 µm
Bit Map of Image

Appendix I: Major Chemical and Mineralogical Components

Component	Fuego[a] (wt. %)	Fuego Groundmass[b] (wt. %)	Spurr[c] (wt. %)	Ash Hollow[d] (wt.%)
SiO_2	51.6	53.0	56.9	75.5
Al_2O_3	20.9	19.0	19.1	11.8
FeO*	8.5	9.2	7.1	2.8
MgO	4.0	3.4	3.6	Trace
CaO	9.8	9.5	7.7	0.6
Na_2O	3.6	3.9	4.0	2.6
K_2O	0.7	0.8	0.9	6.3
TiO_2	0.9	1.2	0.7	0.2
Total	100.0	100.0	100.0	100.0

a. Rose et al., 1978, bulk sample, normalized.
b. Rose et al., 1978, groundmass separates, normalized.
c. Nye et al., 1995, whole rock composition of andesite which does not differ significantly from tan and gray tephra compositions, normalized.
d. Perkins, personal communication, March 2001, normalized.

Volume %	Fuego[a]	Spurr[b] tan	Spurr[b] gray	Ash Hollow
Glass/Groundmass	62.0	68	70	100
Plagioclase	31.0	17	23	0
Hornblende	Trace	1	1	0
Pyroxene	0.8	3	3	0
Magnetite	2.6	0	0	0
Olivine	3.6	0	0	0

a. Rose et al., 1978, bulk sample.
b. Gardner et al., 1998, average volume % determined for gray and tan tephra clasts.

Appendix J: Fuego Shape and Size Parameters

Terminal Velocity (cm/s)	0.6	1.3	2.4	3.7	5.4	7.3	9.5	12.1	14.9	18.0	21.5	25.2	29.2	33.5	38.1	43.1	48.3	53.8	59.0
Combined Means																			
Shape Parameters																			
# of particles	48	63	82	74	79	102	77	67	86	73	55	75	51	61	62	79	68	45	39
Area (μm^2)	41	126	300	499	80	1040	1480	2015	2910	3695	4050	4340	5020	6140	6465	7620	9495	9235	15935
Filled Area (μm^2)	41	126	301	500	830	1040	1480	2040	2940	3740	4100	4410	5080	6180	6550	7695	9675	9340	16395
Perimeter (μm)	25	47	71	91	120	140	165	195	235	265	280	285	300	325	330	365	435	370	530
Convex Per (μm)	25	45	70	88	120	130	160	180	220	245	260	265	280	310	320	345	395	350	500
Length (μm)	9	18	27	33	45	50	60	70	80	90	95	100	100	115	120	130	150	130	180
Width (μm)	5	11	17	21	30	30	40	45	55	60	65	65	70	80	80	90	100	90	130
Sphericity	0.8	0.7	0.7	0.7	0.7	0.7	0.7	0.7	0.7	0.7	0.7	0.7	0.7	0.7	0.7	0.7	0.6	0.7	0.7
Aspect Ratio	1.6	1.7	1.6	1.6	1.6	1.6	1.6	1.6	1.5	1.5	1.5	1.5	1.4	1.4	1.5	1.5	1.5	1.5	1.4
Compactness	0.8	0.7	0.7	0.8	0.8	0.7	0.7	0.7	0.8	0.8	0.8	0.8	0.8	0.8	0.8	0.8	0.8	0.8	0.8
Roughness	1.0	1.0	1.0	1.0	1.0	1.0	1.0	0.9	0.9	0.9	0.9	0.9	0.9	1.0	1.0	1.0	0.9	1.0	0.9
Shape Factor	0.7	0.7	0.7	0.7	0.7	0.7	0.7	0.7	0.8	0.8	0.8	0.8	0.8	0.8	0.8	0.8	0.8	0.8	0.8
Reynold's #	0.0	0.0	0.0	0.1	0.1	0.2	0.3	0.5	0.7	1.0	1.2	1.4	1.8	2.3	2.7	3.3	4.2	4.1	6.4
Size Parameters																			
Feret Ave (μm)	8	15	22	28	35	40	50	60	70	80	80	85	90	100	100	110	125	110	160
Str Length (μm)	8	16	23	29	40	45	55	65	80	90	100	95	95	100	105	115	155	120	170
Str Width (μm)	5	8	13	16	20	25	30	30	35	40	40	50	50	60	60	70	65	65	100
Inner Dia (μm)	4	7	12	15	20	20	25	30	35	40	40	45	50	60	60	65	60	60	100
Outer Dia (μm)	10	19	28	35	45	55	65	70	85	100	100	105	110	120	125	135	160	140	190
Circular Dia (μm)	7	12	19	24	30	35	45	50	60	70	70	75	80	90	90	100	110	100	140
Spher Dia (μm)	8	15	23	30	40	45	50	60	75	80	90	90	95	110	110	120	135	120	170
X-proj (μm)	9	15	23	30	40	45	55	65	80	90	95	95	100	110	110	120	140	120	170
Y-proj (μm)	8	15	23	29	40	45	50	65	75	85	90	90	95	105	105	115	140	120	170
Surf Area (μm^2)	200	660	1500	2500	4300	5500	7800	11000	15000	19000	21000	22000	25000	31100	32700	38100	49800	39100	78600

Terminal Velocity (cm/s)	0.6	1.3	2.4	3.7	5.4	7.3	9.5	12.1	14.9	18.0	21.5	25.2	29.2	33.5	38.1	43.1	48.3	53.8	59.0
Vesiculated Means																			
Shape Parameters																			
# of particles	0	0	0	2	7	3	2	13	26	24	24	32	23	19	22	34	35	26	28
Area (μm^2)	0	0	0	314	705	910	1390	1390	2255	2825	4130	4540	5790	6370	6690	7960	10030	7990	16670
Filled Area (μm^2)	0	0	0	317	720	920	1410	2320	2900	3540	4220	4680	5900	6465	6885	820	10325	8160	17305
Perimeter (μm)	0	0	0	80	120	135	190	205	240	270	300	305	335	330	345	385	470	345	550
Convex Per (μm)	0	0	0	74	110	120	155	190	220	240	265	275	305	315	325	360	410	320	510
Length (μm)	0	0	0	26	40	45	55	70	80	90	100	105	110	115	120	130	155	120	190
Width (μm)	0	0	0	19	30	30	40	50	55	60	70	70	80	85	85	90	105	80	135
Sphericity	0	0	0	0.6	0.6	0.6	0.5	0.7	0.6	0.6	0.6	0.6	0.6	0.7	0.7	0.7	0.6	0.7	0.7
Aspect Ratio	0	0	0	1.4	1.5	1.4	1.5	1.3	1.5	1.5	1.5	1.6	1.5	1.4	1.4	1.5	1.5	1.5	1.4
Compactness	0	0	0	0.7	0.7	0.7	0.7	0.8	0.7	0.7	0.7	0.7	0.8	0.8	0.8	0.8	0.7	0.8	0.8
Roughness	0	0	0	0.9	0.9	0.9	0.8	0.9	0.9	0.9	0.9	0.9	0.9	1.0	0.9	0.9	0.9	0.9	0.9
Shape Factor	0	0	0	0.8	0.8	0.8	0.8	0.8	0.8	0.8	0.8	0.7	0.8	0.8	0.8	0.8	0.8	0.8	0.8
Reynold's #	0	0	0	0.0	0.1	0.2	0.3	0.5	0.7	0.9	1.2	1.5	1.9	2.3	2.7	3.4	4.3	3.8	6.6
Size Parameters	0	0	0																
Feret Ave (μm)	0	0	0	24	35	40	50	60	70	75	85	90	100	100	105	115	130	100	165
Str Length (μm)	0	0	0	29	40	50	75	70	85	100	110	110	120	100	110	130	170	115	180
Str Width (μm)	0	0	0	11	20	20	20	30	35	35	40	40	50	65	60	65	60	60	95
Inner Dia (μm)	0	0	0	10	15	20	20	35	35	35	40	45	50	60	60	65	60	55	100
Outer Dia (μm)	0	0	0	28	40	50	60	70	85	95	105	110	120	120	125	140	160	130	195
Circular Dia (μm)	0	0	0	20	30	30	40	55	60	65	70	75	85	90	90	100	110	90	145
Spher Dia (μm)	0	0	0	25	35	40	50	65	70	80	90	90	105	110	110	120	140	110	180
X-proj (μm)	0	0	0	29	40	50	60	70	80	90	100	100	115	115	120	125	155	110	180
Y-proj (μm)	0	0	0	24	40	40	65	70	80	90	95	100	105	100	105	125	150	110	180
Surf Area (μm^2)	0	0	0	1700	3800	4700	7500	11000	15000	18000	22000	24000	29800	31700	33700	40600	53800	33100	83500

Terminal Velocity (cm/s)	0.6	1.3	2.4	3.7	5.4	7.3	9.5	12.1	14.9	18.0	21.5	25.2	29.2	33.5	38.1	43.1	48.3	53.8	59.0
Nonvesiculated Means																			
Shape Parameters																			
# of particles	48	62	80	73	72	99	75	54	60	49	30	43	28	42	40	45	33	19	11
Area (μm^2)	41	126	300	498	835	1040	1480	1960	2950	3820	4030	4190	4390	6035	6340	7365	9020	10935	14055
Filled Area (μm^2)	41	126	300	499	840	1045	1485	1970	2960	3840	4050	4210	4410	6050	6370	7375	9085	10975	14080
Perimeter (μm)	25	47	71	91	120	135	165	190	230	260	270	270	265	325	325	350	410	405	470
Convex Per (μm)	25	45	69	88	115	130	155	180	215	250	255	255	260	310	320	340	380	390	460
Length (μm)	9	18	27	33	45	50	60	70	80	95	95	95	95	115	120	125	145	145	170
Width (μm)	6	11	17	21	30	30	40	40	55	60	65	65	65	80	80	85	95	95	120
Sphericity	0.8	0.7	0.7	0.7	0.7	0.7	0.7	0.7	0.7	0.7	0.7	0.7	0.8	0.7	0.7	0.8	0.7	0.8	0.8
Aspect Ratio	1.6	1.7	1.6	1.6	1.6	1.6	1.7	1.7	1.5	1.6	1.5	1.5	1.4	1.5	1.6	1.5	1.5	1.5	1.4
Compactness	0.8	0.7	0.7	0.8	0.8	0.7	0.7	0.7	0.8	0.8	0.8	0.8	0.8	0.8	0.8	0.8	0.8	0.8	0.8
Roughness	1.0	1.0	1.0	1.0	1.0	1.0	1.0	1.0	0.9	1.0	0.9	1.0	1.0	1.0	1.0	1.0	0.9	1.0	1.0
Shape Factor	0.7	0.7	0.7	0.7	0.7	0.7	0.7	0.7	0.8	0.7	0.8	0.8	0.8	0.8	0.7	0.8	0.8	0.8	0.8
Reynold's #	0.0	0.0	0.0	0.1	0.1	0.2	0.3	0.5	0.7	1.0	1.2	1.4	1.6	2.3	2.6	3.2	4.0	4.6	5.9
Size Parameters																			
Feret Ave (μm)	8	14	22	28	40	40	50	60	70	80	80	80	80	100	100	110	120	125	145
Str Length (μm)	8	16	23	29	40	45	55	65	80	90	90	80	80	100	100	105	135	120	130
Str Width (μm)	5	8	13	16	20	25	30	30	40	45	45	50	55	60	65	70	70	80	105
Inner Dia (μm)	4	7	12	15	20	20	25	30	35	40	40	45	50	55	55	65	65	70	95
Outer Dia (μm)	10	19	28	35	45	55	65	75	85	100	100	100	100	120	130	130	150	155	180
Circular Dia (μm)	7	12	19	24	30	35	40	50	60	70	70	70	75	90	90	95	105	110	130
Spher Dia (μm)	8	15	23	30	40	45	50	60	75	85	85	90	90	105	110	120	130	135	160
X-proj (μm)	9	15	23	30	40	45	55	60	75	85	90	90	85	105	110	115	125	135	155
Y-proj (μm)	8	15	23	29	40	45	50	60	75	85	85	85	90	105	105	110	135	125	140
Surf Area (μm^2)	200	660	1500	2500	4300	5500	7800	10000	15000	20000	21000	21000	21000	31000	32200	36300	46300	48200	66800

Appendix K: Spurr Shape and Size Parameters

Terminal Velocity (cm/s)	0.6	1.3	2.4	3.7	5.4	7.3	9.5	12.1	14.9	18.0	21.5	25.2	29.2	33.5	38.1	43.1	48.3	53.8
Combined Means																		
Shape Parameters																		
# of particles	112	43	79	47	51	61	89	47	45	55	91	145	129	51	49	76	68	59
Area (μm^2)	15	95	304	440	840	1180	1910	2095	3740	5390	6620	4880	5955	7860	9845	8870	10120	12610
Filled Area (μm^2)	15	96	308	449	855	1215	1980	2160	3805	5470	6750	4930	6041	7995	10060	9040	10190	12720
Perimeter (µm)	14	38	76	88	120	145	185	200	250	290	340	275	310	360	400	380	390	435
Convex Per (µm)	14	36	70	81	120	140	180	175	240	280	320	270	300	355	390	370	390	430
Length (µm)	5	14	26	31	40	50	65	65	90	100	120	100	110	130	140	140	140	160
Width (µm)	3	9	17	20	30	35	45	40	60	70	80	70	80	90	100	95	100	115
Sphericity	0.8	0.7	0.7	0.7	0.7	0.7	0.7	0.6	0.7	0.8	0.7	0.8	0.8	0.8	0.8	0.8	0.8	0.8
Aspect Ratio	1.6	1.5	1.5	1.6	1.6	1.5	1.5	1.6	1.6	1.4	1.5	1.5	1.5	1.5	1.5	1.5	1.4	1.4
Compactness	0.8	0.7	0.7	0.7	0.8	0.8	0.8	0.7	0.8	0.8	0.8	0.8	0.8	0.8	0.8	0.8	0.8	0.8
Roughness	1.0	1.0	0.9	0.9	1.0	1.0	1.0	0.9	1.0	1.0	1.0	1.0	1.0	1.0	1.0	1.0	1.0	1.0
Shape Factor	0.8	0.8	0.8	0.8	0.8	0.8	0.8	0.8	0.8	0.8	0.8	0.8	0.8	0.8	0.8	0.8	0.8	0.8
Reynold's #	0.0	0.0	0.0	0.1	0.1	0.2	0.4	0.5	0.8	1.1	1.5	1.5	1.9	2.6	3.2	3.5	4.1	5.1
Size Parameters																		
Feret Ave (µm)	4	12	22	26	40	40	60	55	75	90	100	90	100	110	125	120	120	140
Str Length (µm)	5	13	27	31	40	50	60	70	80	90	105	80	89	105	120	115	110	120
Str Width (µm)	3	7	11	13	20	25	35	30	50	58	65	60	65	75	80	80	90	100
Inner Dia (µm)	2	6	11	13	20	25	30	30	40	54	60	55	60	65	75	70	80	90
Outer Dia (µm)	6	15	28	33	50	55	70	70	95	110	130	105	120	140	150	145	150	170
Circular Dia (µm)	4	10	20	22	30	40	50	50	70	80	90	80	90	100	110	105	110	125
Spher Dia (µm)	5	12	23	27	40	50	60	60	80	100	110	95	105	120	135	130	140	155
X-proj (µm)	5	13	25	29	40	50	60	65	85	100	115	90	105	125	140	130	130	145
Y-proj (µm)	5	12	25	29	40	50	60	70	80	90	110	90	100	110	125	120	120	140
Surf Area (μm^2)	60	420	1600	2100	4400	6000	9900	9800	18000	25000	33000	24000	29000	39000	47600	43700	47400	59200
Vesiculated Means																		
Shape Parameters																		
# of particles	0	3	19	4	13	30	55	26	35	36	78	97	77	44	45	65	36	33
Area (μm^2)	0	172	360	611	860	1270	1930	3315	4080	4790	6820	5230	5995	7990	10175	8900	11800	13790
Filled Area (μm^2)	0	184	372	640	895	1335	2050	3430	4155	4890	6960	5300	6110	8140	10390	9100	11910	13975
Perimeter (µm)	0	62	89	117	130	155	190	275	270	280	345	290	310	360	410	385	430	460
Convex Per (µm)	0	52	79	103	120	140	180	240	260	270	330	280	305	350	395	375	420	455
Length (µm)	0	19	30	38	50	50	70	90	95	100	120	105	110	130	145	140	150	165
Width (µm)	0	14	20	28	30	40	45	60	65	70	85	70	80	90	100	95	110	120
Sphericity	0	0.5	0.6	0.6	0.6	0.7	0.7	0.6	0.7	0.8	0.7	0.8	0.8	0.8	0.7	0.8	0.8	0.8
Aspect Ratio	0	1.2	1.5	1.4	1.6	1.4	1.5	1.5	1.5	1.4	1.5	1.5	1.5	1.5	1.5	1.5	1.4	1.4
Compactness	0	0.7	0.7	0.7	0.7	0.8	0.7	0.7	0.8	0.8	0.8	0.8	0.8	0.8	0.8	0.8	0.8	0.8
Roughness	0	0.8	0.9	0.9	0.9	0.9	0.9	0.9	1.0	1.0	1.0	1.0	1.0	1.0	1.0	1.0	1.0	1.0
Shape Factor	0	0.8	0.8	0.8	0.7	0.8	0.8	0.8	0.8	0.8	0.8	0.8	0.8	0.8	0.8	0.8	0.8	0.8
Reynold's #	0	0.0	0.0	0.8	0.1	0.2	0.4	0.6	0.8	1.1	1.5	1.5	1.9	2.6	3.3	3.5	4.4	5.3
Size Parameters																		
Feret Ave (µm)	0	17	25	33	40	45	60	80	80	90	105	90	100	110	125	120	135	145
Str Length (µm)	0	25	34	44	50	50	65	100	85	80	110	85	90	105	125	115	120	130
Str Width (µm)	0	7	11	14	20	25	30	40	50	60	65	60	65	75	80	80	90	105
Inner Dia (µm)	0	6	12	17	20	30	30	40	45	55	60	55	60	65	75	70	85	95
Outer Dia (µm)	0	21	31	42	50	55	70	95	100	105	130	110	120	140	155	145	160	180
Circular Dia (µm)	0	14	21	28	30	40	50	65	70	80	90	80	90	100	110	105	120	130
Spher Dia (µm)	0	17	26	34	40	50	60	80	90	95	110	100	105	120	140	130	150	160
X-proj (µm)	0	21	28	38	40	50	65	90	90	95	120	95	105	125	145	130	150	155
Y-proj (µm)	0	21	31	41	45	50	65	90	85	90	110	90	100	110	130	120	130	145
Surf Area (μm^2)	0	870	2000	3300	4700	6400	10000	18000	20000	23000	34200	25000	29600	39400	49700	44200	56500	65800
Nonvesiculated Means																		
Shape Parameters																		
# of particles	112	40	59	43	38	31	34	10	10	17	13	47	27	7	3	11	32	26
Area (μm^2)	15	90	286	424	840	1095	1875	670	2830	4300	5440	4190	5615	7050	4900	8660	8230	11115
Filled Area (μm^2)	15	90	288	431	840	1100	1880	670	2845	4305	5450	4190	5615	7090	5085	8700	8260	11125
Perimeter (µm)	14	36	72	85	20	135	175	105	205	260	295	250	290	350	265	365	345	400
Convex Per (µm)	14	35	67	79	115	130	170	100	200	255	295	250	295	350	255	360	350	400
Length (µm)	5	13	25	30	45	50	65	35	75	95	110	95	110	135	90	130	130	150
Width (µm)	3	9	17	19	30	30	40	25	50	65	70	60	75	80	70	95	90	105
Sphericity	0.8	0.7	0.7	0.7	0.8	0.8	0.8	0.7	0.7	0.8	0.8	0.8	0.8	0.8	0.9	0.8	0.9	0.9
Aspect Ratio	1.6	1.5	1.6	1.6	1.6	1.5	1.7	1.8	1.5	1.6	1.5	1.5	1.7	1.3	1.3	1.4	1.4	1.4
Compactness	0.8	0.7	0.8	0.7	0.8	0.8	0.8	0.7	0.7	0.8	0.8	0.8	0.8	0.8	0.8	0.8	0.8	0.9
Roughness	1.0	1.0	0.9	0.9	1.0	1.0	1.0	1.0	0.9	1.0	1.0	1.0	1.0	1.0	1.0	1.0	1.0	1.0
Shape Factor	0.8	0.8	0.8	0.7	0.8	0.7	0.8	0.8	0.7	0.8	0.7	0.8	0.8	0.7	0.8	0.8	0.8	0.8
Reynold's #	0.0	0.0	0.0	0.1	0.1	0.2	0.4	0.3	0.6	1.0	1.4	1.4	1.9	2.5	2.1	3.4	3.6	4.7
Size Parameters																		
Feret Ave (µm)	4	11	21	25	40	40	55	30	60	80	95	80	95	110	80	115	110	130
Str Length (µm)	5	12	24	30	35	40	60	35	65	80	80	65	80	105	80	105	90	100
Str Width (µm)	3	7	12	13	25	25	35	15	40	50	65	60	65	70	50	75	80	100
Inner Dia (µm)	2	6	12	13	20	25	30	15	30	45	55	50	60	60	60	70	75	85
Outer Dia (µm)	6	14	27	32	50	55	70	40	80	100	115	100	115	145	100	140	135	155
Circular Dia (µm)	4	10	18	22	30	35	50	25	55	70	80	70	85	95	75	100	100	120
Spher Dia (µm)	5	12	23	26	40	45	60	30	65	90	100	90	100	115	90	130	125	145
X-proj (µm)	5	12	24	28	40	45	60	35	70	90	100	85	100	125	95	120	110	130
Y-proj (µm)	5	12	24	28	40	45	55	35	65	80	95	80	90	100	90	120	110	125
Surf Area (μm^2)	60	390	1400	2000	4300	5500	9300	3100	12436	21000	28000	20000	27000	38400	21000	41100	38200	51400

Appendix L: Ash Hollow Shape and Size Parameters

Terminal Velocity (cm/s)	0.6	1.3	2.4	3.7	5.4	7.3	9.5	12.1	14.9	18.0
Shape Parameters										
# of particles	142	94	133	69	72	100	92	51	27	74
Area (μm^2)	117	288	559	1545	2020	1935	3040	3980	4815	5070
Filled Area (μm^2)	117	289	561	1555	2045	195	3060	4010	4860	5110
Perimeter (μm)	42	66	91	165	190	240	275	310	300	300
Convex Per (μm)	42	65	89	160	185	180	230	265	290	290
Length (μm)	16	26	35	60	75	70	90	105	120	120
Width (μm)	10	15	20	35	40	40	50	55	60	60
Sphericity	0.8	0.7	0.7	0.6	0.6	0.6	0.6	0.6	0.6	0.6
Aspect Ratio	1.6	1.8	1.8	1.9	2.0	2.1	2.3	2.2	2.6	2.5
Compactness	0.7	0.7	0.7	0.7	0.6	0.6	0.7	0.7	0.6	0.6
Roughness	1.0	1.0	1,0	1.0	1.0	1.0	1.0	1.0	1.0	1.0
Shape Factor[a]	0.7	0.7	0.7	0.7	0.7	0.7	0.7	0.7	0.6	0.6
Reynold's #	0.0	0.0	0.0	0.1	0.2	0.3	0.5	0.7	1.0	1.1
Size Parameters										
Feret Ave (μm)	13	21	28	50	60	60	75	85	95	90
Str Length (μm)	13	22	31	55	70	70	85	100	115	110
Str Width (μm)	8	11	15	25	30	30	35	40	40	40
Inner Dia (μm)	7	11	14	25	25	25	30	40	40	40
Outer Dia (μm)	17	27	37	65	80	80	100	110	125	125
Circular Dia (μm)	11	17	23	40	45	45	60	70	70	70
Spher Dia (μm)	14	21	29	50	60	55	70	80	90	90
X-proj (μm)	13	22	30	55	60	60	80	90	110	105
Y-proj (μm)	14	21	30	50	60	65	75	90	90	90
Surf Area[b] (μm^2)	550	1400	2500	8000	11000	110000	17000	22000	27000	27000

a. Wilson and Huang, 1979.

b. Surface area of a sphere is $\pi(\text{feret average})^2$

Appendix M: Comparison Between Feret and Spherical Particle Diameters

Fuego

Ter. Vel. (cm/s)	Calculated Equivalent Spherical Diameters (µm)		Actual Feret Diameter (µm)	Percent Smaller or Larger Than Spherical Diameter	
	ρ = 2.4 g/cm^3	**ρ = 2.6 g/cm^3**		**ρ = 2.4 g/cm^3**	**ρ = 2.6 g/cm^3**
0.6	0	0	0	0	0
1.3	9	9	8	-14	-11
2.4	14	13	15	6	10
3.7	18	18	22	21	26
5.4	23	22	30	23	28
7.3	27	26	35	35	40
9.5	32	31	40	31	36
12.1	36	35	50	37	42
14.9	41	39	60	41	47
18.0	46	44	70	51	57
21.5	50	48	80	56	62
25.2	55	53	80	50	57
29.2	59	57	85	41	47
33.5	64	61	90	40	45
38.1	68	66	100	46	52
43.1	73	70	100	40	46
48.3	77	74	110	42	48
53.8	82	79	125	54	60
59	87	83	110	29	34

Spurr

Ter. Vel. (cm/s)	Calculated Equivalent Spherical Diameters (µm)			Actual Feret Diameter (µm)	Percent Smaller or Larger Than Spherical Diameter		
	ρ = 1.5 g/cm^3	**ρ = 2.3 g/cm^3**	**ρ = 2.7 g/cm^3**		**ρ = 1.5 g/cm^3**	**ρ = 2.3 g/cm^3**	**ρ = 2.7 g/cm^3**
0.6	12	9	9	4	-62	-53	-49
1.3	17	14	13	12	-33	-17	-10
2.4	23	19	17	22	-4	19	29
3.7	29	23	21	26	-10	11	21
5.4	35	28	26	40	9	34	46
7.3	40	33	30	45	8	34	45
9.5	46	37	34	55	22	51	63
12.1	52	42	39	55	8	33	44
14.9	58	47	43	75	32	63	77
18.0	63	51	47	90	40	73	87
21.5	69	56	52	100	49	84	100
25.2	75	60	56	85	16	43	55
29.2	81	65	60	95	19	47	60
33.5	86	70	64	110	29	60	74
38.1	92	74	69	125	33	65	79
43.1	98	79	73	120	21	49	62
48.3	104	84	77	120	18	47	59
53.8	109	88	82	140	25	55	68

Ash Hollow

Ter. Vel. (cm/s)	Calculated Equivalent Spherical Diameters (µm)		Actual Feret Diameter (µm)	Percent Smaller or Larger Than Spherical Diameter	
	ρ = 2.3 g/cm^3	**ρ = 2.7 g/cm^3**		**ρ = 2.3 g/cm^3**	**ρ = 2.7 g/cm^3**
0.6	9	9	13	43	55
1.3	14	13	21	49	61
2.4	19	17	28	52	65
3.7	23	21	50	117	135
5.4	28	26	60	112	129
7.3	33	30	60	78	93
9.5	37	34	75	97	114
12.1	42	39	85	101	117
14.9	47	43	95	100	117
18.0	51	47	90	81	96